Equilibrium quasicrystal phase of a Penrose tiling model

Lei-Han Tang* and Marko V. Jarić
Center for Theoretical Physics, Texas A&M University, College Station, Texas 77843
(Received 7 August 1989)

A two-dimensional rhombus tiling model with a matching-rule-based energy is analyzed using real-space renormalization-group methods and Monte Carlo simulations. The model spans a range from $T=0$ quasiperiodic crystal (Penrose tiling) to a random-tiling quasicrystal at high temperatures. A heuristic picture for the disordering of the ground-state quasiperiodicity at low temperatures is proposed and corroborated with exact and renormalization-group calculations of the phason elastic energy, which shows a linear dependence on the strain at $T=0$ but changes to a quadratic behavior at $T>0$ and sufficiently small strain. This is further supported by the Monte Carlo result that phason fluctuations diverge logarithmically with system size for all $T>0$, which indicates the presence of quasi-long-range translational order in the system, meaning algebraically decaying correlations. A close connection between the rhombus tiling model and the general surface-roughening phenomena is established. Extension of the results to three dimensions and their possible implication to experimental systems is also addressed.

I. INTRODUCTION

Quasicrystals represent a new form of ordered state, characterized by sharp diffraction peaks with noncrystallographic symmetry.[1-6] Immediately after the first report in the icosahedral phase in Al and transition-metal alloys by Shechtman *et al.*[1] Levine and Steinhardt[2] proposed *quasiperiodic* crystals as the ideal structural model for these systems. It is assumed that in these materials there exist microscopic forces that lead to the formation of stable quasiperiodic structures.[7] Although the presence and physical origin of these forces in any particular experimental system are yet to be elucidated, the well-known two-dimensional (2D) and three-dimensional (3D) Penrose tilings provide working examples of quasiperiodic patterns for which the matching rules conceptually represent such microscopic forces.[7-10]

At the same time, Elser and Henley made a microscopically different, but physically equally plausible proposal for the structure of equilibrium quasicrystals, known as the "random-tiling model."[11-16] As the name implies, a quasicrystal in this picture is viewed as a *random* packing of two or more different kinds of rigid geometrical units which fill the whole space. Each such unit consists of a certain number of tightly bonded atoms, but unlike the case in a quasiperiodic crystal, the same energy is assigned to all possible local tiling configurations.[13,14] In such a system, the equilibrium state is determined by the entropy associated with tile rearrangements. It was conjectured that quasicrystal arrangements, i.e., those tilings whose Fourier transforms show sharp peaks and a high, but noncrystallographic symmetry, possess maximal entropy, and are thus favored.[11,12]

Although the random-tiling scenario does not rely on the existence of a quasiperiodic ground state, it is intuitively clear that under suitable conditions it may correspond to a high-temperature phase of a quasiperiodic crystal model in which two or more "unit cells" are packed quasiperiodically. The study of such a model is important not only for clarifying the distinction between the two proposals, but also for gaining a better understanding of the equilibrium quasicrystal phase over a broad range of temperatures.

In this paper we explore the thermal equilibrium properties of 2D rhombus tilings of 36° and 72° rhombuses. The energy of a given tiling is defined according to a set of matching rules introduced by Penrose, which will be specified in detail in Sec. II A. The ground state of the model consists of the Penrose tilings, which satisfy the matching rules everywhere. At infinite temperature the matching-rule energies become irrelevant so that a random-rhombus-tiling ensemble is achieved.

Such a model is perhaps too simple to be an accurate description of a real physical system. For sure, it completely ignores phonon modes which would be associated with tile distortions. By insisting on rigid tiles, one also excludes the possibility of dislocations and other defects which couple to phonons.[17] In addition, the model as we defined it does not contain a dynamical description for tile rearrangements.

Despite the aforementioned limitations, the model does have several attractive features. First of all, the ground state of the system is known. We note that finding an incommensurate ground state of even a classical one-dimensional system is a nontrivial problem.[18,19] Knowing the ground state enables us to analyze the equilibrium processes at low temperatures, which are the tile rearrangements, normally described as phason fluctuations.[17] Secondly, the matching-rule-based energetics offers a new class of incommensurate systems which have not been studied in detail before. Such rules are usually absent in systems modulated in one direction, e.g., the Frenkel-Kontorova model and the axial-next-nearest-neighbor Ising (ANNNI) model.[18-23] There, different incommensurate ground states are often stabilized by tiny interactions between domain-wall-type defects. As a result, each of

them has zero volume on the phase diagram. In our model, the quasicrystal phase is expected to occupy a finite volume on the phase diagram when plotted under proper parameters. In addition, the nice inflation symmetry of the ground-state Penrose tilings[8,24–27] allows us to develop a simple real-space renormalization scheme so that the melting of ground-state quasiperiodicity can be conveniently analyzed.

There exists a simple mapping of vertices of the rhombus tiling to a subset of five-dimensional (5D) hypercubic lattice sites which form a continuous 2D hypersurface.[12] Under this mapping, a Penrose tiling corresponds to a macroscopically flat hypersurface, which is macroscopically invariant under the fivefold symmetry operation of the 5D hypercubic lattice. Rearrangements of tiles away from the Penrose tiling lead to fluctuations of the hypersurface. These fluctuations are usually described in terms of the "phason variables," which give the coordinates of the hypersurface along directions perpendicular to the flat surface.[3,7,28]

It has been recognized that the presence or absence of long-range translational order in a quasicrystal is determined by whether the representing hypersurface is flat or rough. Fluctuations of the hypersurface are governed by the energetics of the quasicrystal. An important question which arises under this context is whether such a hypersurface can become rough due to thermal fluctuations.

The roughening of an ordinary solid-gas interface along one of the major crystal symmetry directions usually occurs at a finite temperature $T_R > 0$.[29–32] An important quantity which characterizes the transition is the free energy for slightly tilted interfaces. Below T_R, this free energy depends linearly on the tilt angle, and gives rise to a cusp on the Wulff plot. This behavior is intuitively understood as due to the breaking of translational symmetry in the surface height direction by the crystal lattice, such that a linear height gradient can only be distributed on a set of steps. At $T > T_R$, a quadratic surface free energy is obtained, from which surface height fluctuations can be calculated. These fluctuations usually diverge logarithmically with increasing system size.

In quasicrystals one can define a phason elastic (free) energy which plays the same role as the surface free energy. At $T=0$, Socolar *et al.* suggested a linear dependence of the elastic energy on phason strain for unit-cell quasicrystals with matching-rule-based energies.[17] This is somewhat surprising in view of the fact that quasicrystals have a continuous symmetry resulting from the energy invariance under uniform "phason translations."[3,28,33] In the random-tiling case a quadratic free energy was conjectured by Elser and Henley,[11,12] and confirmed by transfer-matrix studies of Widom *et al.*,[15] and Monte Carlo simulations of Strandburg *et al.*[16] (part of the work is reported in detail here). As a consequence, 2D random tilings have "quasi-long-range" translational order, characterized by algebraically decaying correlation functions and power-law diffraction peaks.

A similar situation is expected in more physical models. Consider, for example, a ground-state quasiperiodic crystal resulting from short-range pairwise interactions between the atoms. Then, it can be shown that certain general assumptions about the associated atomic hypersurfaces imply a singular, linear phason elasticity at $T=0$.[34] On the other hand, finite-temperature density-functional calculations for atomic models are consistent with the quadratic phason elastic energy.[35]

This raises the question about the nature of the transition between the singular, linear, and the quadratic phason elasticity regimes. Therefore, in the context of the Penrose tiling, the focus of the present paper will be the following questions. What is the roughening temperature of a 2D equilibrium quasicrystal? How does the roughening transition take place? Is the quadratic free-energy description valid for the thermal fluctuations of the representing hypersurface in the rough phase?

The remaining part of the paper is organized as follows. In Sec. II we introduce a matching-rule-based energy defined on rhombus tilings. This is followed by a review of the 5D representation of rhombus tilings and the definition of phason variables. We then discuss the Fourier transform properties for tilings with or without phason strain. In the last part of Sec. II we outline the main results obtained by assuming a square-gradient free energy for long-wavelength phason fluctuations.

In Sec. III we study the zero-temperature phason elastic energy of the model. By using simple geometrical relations we obtain a rigorous lower bound for the strain energy, which shows a linear dependence on an overall scale change of the strain tensor. This lower bound becomes an exact expression for a restricted class of tilings.

Section IV contains a heuristic discussion on the thermal roughening of the hypersurface representing a quasicrystal. Special attention will be given to the step free energy. The usual argument for the roughening of a crystal surface, when applied to the incommensurately oriented hypersurface, suggests a zero-temperature roughening transition.

In Sec. V we present a real-space renormalization-group (RG) analysis based on a generalization of the inflation transformation on the Penrose tilings. An approximate RG equation for the fugacity of matching-rule violations is derived. We find that, in the quasicrystal phase, the equilibrium distribution at any nonzero temperature flows toward the infinite-temperature random-tiling limit under successive RG transformations. The analysis indicates that a low temperature tiling behaves like a random tiling on sufficiently large length scales. This again suggests a zero-temperature roughening transition. The free energy for tilings with and without phason strain is approximately calculated, which shows two different kinds of behavior depending on the temperature and phason strain. The analysis also gives the dependence of phason elastic constant on temperature in the rough phase.

In Sec. VI we present results from a detailed Monte Carlo study of three limiting cases of the rhombus-tiling model. The result confirms the existence of quasi-long-range translational order in the random-tiling models, and in the quasiperiodic crystal model at finite temperatures. In the latter case, the logarithmic divergence of phason fluctuations on system size continues down to very low temperatures, only limited by the size of system

studied. This provides yet another evidence for the zero-temperature roughening transition. The temperature dependence of energy and elastic constant agree to leading order with results of the RG calculation given in Sec. V. In Sec. VII we summarize our results and discuss an extension of the analysis to three dimensions, and point out some possible applications to experimental systems. The Appendix contains an exact calculation of energy per vertex for a special class of tilings at $T=0$.

II. DEFINITION AND BASIC PROPERTIES

A. The model

Consider a plane-filling tiling by arrowed skinny (36°) and fat (72°) rhombuses shown in Fig. 1(a). Viewing each rhombus as a unit cell, the spatial pattern defines a network of vertices connected by bonds, which are the rhombus edges in the tiling. On each bond reside two arrows, whose types (single, double) and direction give rise to six possible states to the bond, as illustrated in Fig. 1(b). The following shorthand notation will be used to denote the state of the bond: *SS* for two single arrows, *DD* for two double arrows, and *SD* for a single and a double arrow. In addition, each such combination is given a superscript "+" if the two arrows are parallel, and a superscript "−" otherwise. States $(SS)^+$ and $(DD)^+$ are referred to as *matched,* and the rest, *unmatched.*

A simple statistical mechanical model on the tilings, we call the *Penrose model,* is introduced by assigning an energy to each bond,

$$\varepsilon_b=\begin{cases}0 \text{ for } (SS)^+ \text{ and } (DD)^+ \text{ states},\\ \varepsilon_{SS} \text{ for } (SS)^- \text{ state},\\ \varepsilon_{DD} \text{ for } (DD)^- \text{ state},\\ \varepsilon_{SD} \text{ for } (SD)^+ \text{ and } (SD)^- \text{ states}.\end{cases} \tag{2.1}$$

The energy of a tiling χ is (formally) defined as a sum of bond energies

$$E(\chi)=\sum_{\text{bonds}}\varepsilon_b\ . \tag{2.2}$$

In this paper we shall consider only the case where ε_{SS}, ε_{DD}, and ε_{SD} are all positive.

The ground states of the above model are tilings which contain no unmatched arrows. Penrose discovered the set of such tilings over ten years ago.[8] It was later shown by deBruijn that the Penrose tilings are quasiperiodic.[24]

Additional terms, such as vertex energies, can be incorporated in Eq. (2.2) to accommodate a more general class of rhombus-tiling models. For instance, the *binary tilings,* derived from the quasicrystal phase of a 2D, two-component Lennard-Jones system,[13,14] can be represented by assigning zero energy to vertices at which the corner angles of surrounding rhombuses are either all even or all odd multiples of $\pi/5$, and infinite energy to all other types of vertices. These additional terms may introduce competing interactions in the energy, in which case, finding the ground state of the system may become a highly nontrivial problem.

B. Five-dimensional representation of tiling structures

The geometrical properties of a rhombus tiling are most conveniently discussed by lifting the vertex network to a higher-dimensional space. The mathematical procedure for the mapping is illustrated in Fig. 2. In the tiling each rhombus edge is oriented in one of the five directions

$$\hat{\mathbf{e}}^{\parallel}_{\alpha}=(\cos 2\pi\alpha/5,\sin 2\pi\alpha/5),\quad \alpha=0,\ldots,4\ . \tag{2.3}$$

Choosing an arbitrary vertex O as the origin, the position of any other vertex of the tiling is expressed as

$$\mathbf{r}=a\sum_{\alpha=0}^{4} n_\alpha \hat{\mathbf{e}}^{\parallel}_{\alpha}\ , \tag{2.4}$$

where a is the length of a rhombus edge, and n_α is the number of steps in direction $\hat{\mathbf{e}}^{\parallel}_{\alpha}$ on a continuous path to

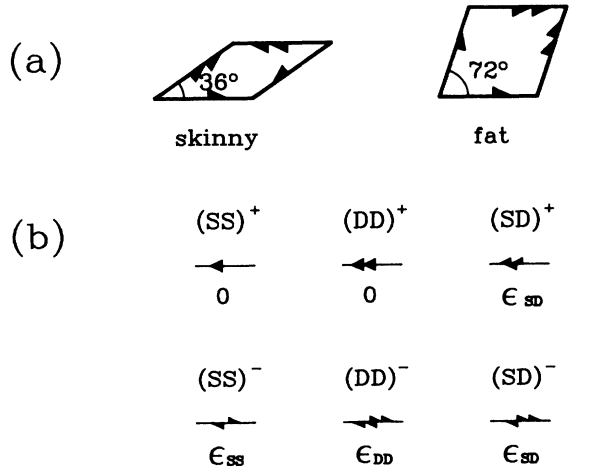

FIG. 1. (a) 36° (skinny) and 72° (fat) rhombuses decorated with single (S) and double (D) arrows. (b) Six possible arrow configurations on a bond and their energy ε_b. The superscript "+" indicates two arrows on a bond are parallel, and "−," opposite.

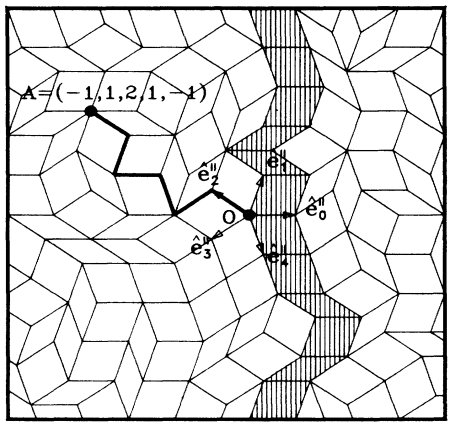

FIG. 2. Definition of 5D coordinates of vertices. A path from an arbitrarily chosen origin O to a vertex A is shown by the heavy line. The shaded part is a row of tiles.

the vertex at $\mathbf{r}$ from the origin along the bonds, counting negatively when going in the opposite direction. For instance, the point A in Fig. 2 has $\{n_\alpha\}=(-1,1,2,1,-1)$. Despite the fact that the five vectors $\hat{\mathbf{e}}_\alpha^{\parallel}$ sum to zero, this procedure gives a unique definition of $\{n_\alpha\}$ once the origin is chosen, independent of the path taken.

Taking $\{n_\alpha\}$ as 5D coordinates, the vertices of a rhombus tiling are made to correspond to a subset of 5D hypercubic lattice sites. The 5D hypercubic lattice has a fivefold symmetry, under whose operation the 5D space decomposes into three invariant subspaces: a 2D "physical space" spanned by basis vectors

$$\begin{aligned}\hat{\mathbf{a}}^{(1)}&=\sqrt{2/5}\left[1,\cos\frac{2\pi}{5},\cos\frac{4\pi}{5},\cos\frac{6\pi}{5},\cos\frac{8\pi}{5}\right]\\&\equiv\sqrt{2/5}\left\{\cos\frac{2\pi\alpha}{5}\right\},\\\hat{\mathbf{a}}^{(2)}&=\sqrt{2/5}\left[0,\sin\frac{2\pi}{5},\sin\frac{4\pi}{5},\sin\frac{6\pi}{5},\sin\frac{8\pi}{5}\right]\\&\equiv\sqrt{2/5}\left\{\sin\frac{2\pi\alpha}{5}\right\},\end{aligned}\tag{2.5}$$

a 2D "perpendicular space" spanned by basis vectors

$$\begin{aligned}\hat{\mathbf{a}}^{(3)}&=\sqrt{2/5}\left[1,\cos\frac{4\pi}{5},\cos\frac{8\pi}{5},\cos\frac{12\pi}{5},\cos\frac{16\pi}{5}\right]\\&\equiv\sqrt{2/5}\left\{\cos\frac{4\pi\alpha}{5}\right\},\\\hat{\mathbf{a}}^{(4)}&=\sqrt{2/5}\left[0,\sin\frac{4\pi}{5},\sin\frac{8\pi}{5},\sin\frac{12\pi}{5},\sin\frac{16\pi}{5}\right]\\&\equiv\sqrt{2/5}\left\{\sin\frac{4\pi\alpha}{5}\right\},\end{aligned}\tag{2.6}$$

and a one-dimensional "perpendicular space" along the (commensurate) fivefold symmetry axis

$$\hat{\mathbf{a}}^{(5)}=\sqrt{1/5}(1,1,1,1,1)\equiv\sqrt{1/5}\{1\}\ .\tag{2.7}$$

The original tiling is recovered by projecting the subset of hypercubic lattice sites $\mathbf{R}=\{n_\alpha\}$ onto the physical space, i.e.,

$$\begin{aligned}\mathbf{r}&=a\sqrt{5/2}\mathbf{R}^{\parallel}\\&=a\sqrt{5/2}[(\mathbf{R}\cdot\hat{\mathbf{a}}^{(1)})\hat{\mathbf{a}}^{(1)}+(\mathbf{R}\cdot\hat{\mathbf{a}}^{(2)})\hat{\mathbf{a}}^{(2)}]\ ,\end{aligned}\tag{2.8}$$

and connecting vertices separated by a distance a with bonds. Projection of $\mathbf{R}$ onto the other two invariant subspaces gives the perpendicular-space (or phason) coordinates

$$\begin{aligned}\mathbf{h}(\mathbf{r})&\equiv\sqrt{5/2}[(\mathbf{R}\cdot\hat{\mathbf{a}}^{(3)})\hat{\mathbf{a}}^{(3)}+(\mathbf{R}\cdot\hat{\mathbf{a}}^{(4)})\hat{\mathbf{a}}^{(4)}]\\&=\sum_{\alpha=0}^{4}n_\alpha\hat{\mathbf{e}}_\alpha^{\perp}\ ,\\h_z(\mathbf{r})&\equiv\sqrt{5}\mathbf{R}\cdot\hat{\mathbf{a}}^{(5)}=\sum_{\alpha=0}^{4}n_\alpha\ .\end{aligned}\tag{2.9}$$

Here

$$\hat{\mathbf{e}}_\alpha^{\perp}=(\cos4\pi\alpha/5,\sin4\pi\alpha/5)\ .\tag{2.10}$$

Each rhombus in the tiling is a projection of a square face of a 5D hypercube. These square faces connect into a 2D surface imbedded in the 5D space, and the entire 2D tiling can be viewed as a projection of this surface onto the 2D physical space. We shall call this surface the *deBruijn surface*. For a Penrose tiling, the average orientation of the deBruijn surface is the same as the orientation of the physical space. In general, a deBruijn surface can have a *different* average orientation, in which case we say the corresponding tiling has a uniform *phason strain*. The phason strain matrices $\mathbf{E}$ and $\mathbf{E}_z$ are defined through

$$\mathbf{E}=a[\langle\mathbf{h}(\mathbf{r})\mathbf{r}\rangle-\mathbf{h}^0\langle\mathbf{r}\rangle]\langle\mathbf{r}\mathbf{r}\rangle^{-1}\ ,\tag{2.11}$$

and

$$\mathbf{E}_z=a[\langle h_z(\mathbf{r})\mathbf{r}\rangle-h_z^0\langle\mathbf{r}\rangle]\langle\mathbf{r}\mathbf{r}\rangle^{-1}\ ,\tag{2.12}$$

where we used the dyad notation. Here $\langle\ \rangle$ denotes averaging over all vertices of the tiling, and the uniform phason displacements are $\mathbf{h}^0=\langle\mathbf{h}(\mathbf{r})\rangle$ and $h_z^0=\langle h_z(\mathbf{r})\rangle$. The average orientation of the deBruijn surface is then specified by two vectors

$$\begin{aligned}\mathbf{b}^{(1)}&=\hat{\mathbf{a}}^{(1)}+E_{11}\hat{\mathbf{a}}^{(3)}+E_{21}\hat{\mathbf{a}}^{(4)}+\frac{1}{\sqrt{2}}E_{z1}\hat{\mathbf{a}}^{(5)}\ ,\\\mathbf{b}^{(2)}&=\hat{\mathbf{a}}^{(2)}+E_{12}\hat{\mathbf{a}}^{(3)}+E_{22}\hat{\mathbf{a}}^{(4)}+\frac{1}{\sqrt{2}}E_{z2}\hat{\mathbf{a}}^{(5)}\ ,\end{aligned}\tag{2.13}$$

both parallel to the deBruijn surface. Here E_{ij} and E_{zj}, $i,j=1,2$, are matrix elements of $\mathbf{E}$ and $\mathbf{E}_z$, respectively. (We note that, like the ordinary elastic strain of a solid, the phason strain can be defined locally under a suitable continuum limit.)

For the following discussion it is useful to distinguish rhombuses (fat or skinny) oriented in each of the five possible directions. The *type* of a rhombus is specified by two subscripts (α,β) of the edge vectors $a\hat{\mathbf{e}}_\alpha^{\parallel}$ and $a\hat{\mathbf{e}}_\beta^{\parallel}$, which form the rhombus. The choice $\beta=\alpha+1$ (mod 5) gives a fat rhombus, while $\beta=\alpha+2$ (mod 5) gives a skinny rhombus. The average number density $\rho_{(\alpha,\beta)}$ of rhombuses of type (α,β) exists for a uniformly strained tiling, and is uniquely determined by $\mathbf{E}$ and $\mathbf{E}_z$ as follows.

An (α,β) rhombus corresponds to a 2D square face of a 5D hypercube with edges parallel to the α and β axes. As mentioned above, a tiling can thus be visualized as a corrugated 2D deBruijn surface in the 5D space. The projected area of the deBruijn surface onto the $\alpha\beta$ plane gives the number of 2D faces associated with (α,β) rhombus, contained in the deBruijn surface. From this observation we obtain the density of (α,β) rhombuses:

$$\rho_{(\alpha,\beta)}=\frac{2}{5a^2}\frac{|(b_\alpha^{(1)},b_\beta^{(1)})\times(b_\alpha^{(2)},b_\beta^{(2)})|}{|\mathbf{b}^{(1)\parallel}\times\mathbf{b}^{(2)\parallel}|}$$
$$=\frac{4}{25a^2}\left[\sin\frac{2\pi(\beta-\alpha)}{5}+\hat{\mathbf{e}}_\alpha^{\parallel}\times(\mathbf{E}^T\hat{\mathbf{e}}_\beta^{\perp})-\hat{\mathbf{e}}_\beta^{\parallel}\times(\mathbf{E}^T\hat{\mathbf{e}}_\alpha^{\perp})+\tfrac{1}{2}(\hat{\mathbf{e}}_\alpha^{\parallel}-\hat{\mathbf{e}}_\beta^{\parallel})\times\mathbf{E}_z^T\right.$$
$$\left.+\sin\frac{4\pi(\beta-\alpha)}{5}\det\mathbf{E}+\tfrac{1}{2}[\mathbf{E}^T(\hat{\mathbf{e}}_\alpha^{\perp}-\hat{\mathbf{e}}_\beta^{\perp})]\times\mathbf{E}_z^T\right]. \tag{2.14}$$

Here $\mathbf{b}^{(1)\parallel}$ and $\mathbf{b}^{(2)\parallel}$ are the projections of $\mathbf{b}^{(1)}$ and $\mathbf{b}^{(2)}$ onto the physical space, and $\mathbf{E}^T$ and $\mathbf{E}_z^T$ are the transpose of $\mathbf{E}$ and $\mathbf{E}_z$, respectively. The overall density of fat and skinny rhombuses are given by

$$\rho_F=\sum_{\alpha=0}^{4}\rho_{(\alpha,\alpha+1)}=\frac{4}{5a^2}\left[\sin\frac{2\pi}{5}+\tau^{-1}\sin\frac{2\pi}{5}\det\mathbf{E}\right],$$
$$\rho_S=\sum_{\alpha=0}^{4}\rho_{(\alpha,\alpha+2)}=\frac{4}{5a^2}\left[\tau^{-1}\sin\frac{2\pi}{5}-\sin\frac{2\pi}{5}\det\mathbf{E}\right], \tag{2.15}$$

respectively. Here $\tau=(\sqrt{5}+1)/2$ is the golden mean. The total density of rhombuses, which is the same as the density of vertices, is given by the sum $\rho_F+\rho_S$. Equations (2.14) and (2.15) have been derived previously by Henley for the case $\mathbf{E}_z=0$.[12]

C. Fourier properties and long-range translational order

Simple as they are, the rhombus tilings can exhibit a variety of spatial patterns, amongst which are periodic configurations with arbitrarily large unit cells, quasiperiodic configurations, and random configurations, and give rise to distinct diffraction patterns. Quite generally, each scattering peak can be indexed with five integers, corresponding to a reciprocal-lattice vector

$$\mathbf{Q}=\{2\pi m_\alpha\} \tag{2.16}$$

of the 5D hypercubic lattice. (This indexing is not unique if the deBruijn surface representing the tiling is oriented commensurately along one or more directions of the 5D hypercubic lattice.) For example, the peak position of the Penrose tilings is given by the projection of $\mathbf{Q}$ onto the physical space

$$\mathbf{Q}_P^{\parallel}=\frac{4\pi}{5a}\sum_\alpha m_\alpha\hat{\mathbf{e}}_\alpha^{\parallel}, \tag{2.17}$$

where a is the rhombus edge length, and the indexing is unique mod(1,1,1,1,1).

In general, for a tiling with uniform phason strain $\mathbf{E}$ and $\mathbf{E}_z$, we consider a scattering wave vector

$$\mathbf{Q}^{\parallel}=\mathbf{Q}_P^{\parallel}+\Delta\mathbf{Q}^{\parallel}. \tag{2.18}$$

At an arbitrary vertex $\mathbf{r}=a\sum_\alpha n_\alpha\hat{\mathbf{e}}_\alpha^{\parallel}$, we have

$$\mathbf{Q}^{\parallel}\cdot\mathbf{r}=\mathbf{Q}_P^{\parallel}\cdot\mathbf{r}+\Delta\mathbf{Q}^{\parallel}\cdot\mathbf{r}$$
$$=2\pi\sum_\alpha m_\alpha n_\alpha-\mathbf{Q}_P^{\perp}\cdot\mathbf{h}(\mathbf{r})-Q_{Pz}h_z(\mathbf{r})+\Delta\mathbf{Q}^{\parallel}\cdot\mathbf{r}$$
$$=2\pi\sum_\alpha m_\alpha n_\alpha-\mathbf{Q}_P^{\perp}\cdot\tilde{\mathbf{h}}(\mathbf{r})-Q_{Pz}\tilde{h}_z(\mathbf{r})$$
$$+(\Delta\mathbf{Q}^{\parallel}-a^{-1}\mathbf{E}^T\mathbf{Q}_P^{\perp}-a^{-1}\mathbf{E}_z^TQ_{Pz})\cdot\mathbf{r}, \tag{2.19}$$

where

$$\mathbf{Q}_P^{\perp}=\frac{4\pi}{5}\sum_\alpha m_\alpha\hat{\mathbf{e}}_\alpha^{\perp},$$
$$Q_{Pz}=\frac{2\pi}{5}\sum_\alpha m_\alpha, \tag{2.20}$$

are the perpendicular-space components of $\mathbf{Q}$, and

$$\tilde{\mathbf{h}}(\mathbf{r})=\mathbf{h}(\mathbf{r})-a^{-1}\mathbf{E}\mathbf{r},$$
$$\tilde{h}_z(\mathbf{r})=h_z(\mathbf{r})-a^{-1}\mathbf{E}_z\mathbf{r}, \tag{2.21}$$

denote fluctuations of the deBruijn surface from its average position.

The last term in Eq. (2.19) vanishes if we take

$$\Delta\mathbf{Q}^{\parallel}=a^{-1}(\mathbf{E}^T\mathbf{Q}_P^{\perp}+\mathbf{E}_z^TQ_{Pz}). \tag{2.22}$$

The structure factor at $\mathbf{Q}^{\parallel}$ for a system of N vertices (or equivalently, N tiles), is then given by

$$S_N(\mathbf{Q}^{\parallel})=\sum_{\mathbf{r}}\exp(i\mathbf{Q}^{\parallel}\cdot\mathbf{r})$$
$$=\sum_{\mathbf{r}}\exp[-i\mathbf{Q}_P^{\perp}\cdot\tilde{\mathbf{h}}(\mathbf{r})-iQ_{Pz}\tilde{h}_z(\mathbf{r})], \tag{2.23}$$

where the sum is carried out over all vertices. From this we obtain the scattering intensity at $\mathbf{Q}^{\parallel}$,

$$I_N(\mathbf{Q}^{\parallel})=|S_N(\mathbf{Q}^{\parallel})|^2/N$$
$$=\sum_{\mathbf{r}}\exp\{-i\mathbf{Q}_P^{\perp}\cdot[\tilde{\mathbf{h}}(\mathbf{r})-\tilde{\mathbf{h}}(\mathbf{0})]$$
$$-iQ_{Pz}[\tilde{h}_z(\mathbf{r})-\tilde{h}_z(\mathbf{0})]\}. \tag{2.24}$$

Equation (2.24) shows that if the differences $\tilde{\mathbf{h}}(\mathbf{r})-\tilde{\mathbf{h}}(\mathbf{0})$ and $\tilde{h}_z(\mathbf{r})-\tilde{h}_z(\mathbf{0})$ remain bounded throughout the system, which means that the deBruijn surface is *flat* on large length scales, Bragg scattering peaks are obtained. Tilings with this property are said to possess long-range translational order.

Unbounded fluctuations of $\tilde{\mathbf{h}}$ and $\tilde{h}_z$, which describe the behavior of a *rough* deBruijn surface, can destroy the Bragg scattering peaks, hence the long-range translation-

al order in the system.

Finally, we consider an alternative, perhaps more direct way of analyzing the translational order in a tiling. Let us call a *row* to be a stack of abutting tiles in a rhombus tiling, as illustrated by the shaded part in Fig. 2. A row is said to belong to set α if the tiles are stacked on edges parallel to $\hat{\mathbf{e}}_\alpha^{\parallel}$. ($\alpha=0$ for the example shown in Fig. 2.) For a tiling with zero phason strain, the average orientation of a row of set α is normal to $\hat{\mathbf{e}}_\alpha^{\parallel}$. Let $\mathbf{r}_1$ and $\mathbf{r}_2$ be two vertices of the tiling with 5D coordinates $\{n_\beta^1\}$ and $\{n_\beta^2\}$. Then

$$\Delta\mathbf{r}\cdot\hat{\mathbf{e}}_\alpha^{\parallel}=(\mathbf{r}_2-\mathbf{r}_1)\cdot\hat{\mathbf{e}}_\alpha^{\parallel}=a\left(\tfrac{5}{2}\Delta n_\alpha-\Delta\mathbf{h}\cdot\hat{\mathbf{e}}_\alpha^{\perp}-\tfrac{1}{2}\Delta h_z\right) . \quad (2.25)$$

By choosing both $\mathbf{r}_1$ and $\mathbf{r}_2$ to be on the same row α, $\Delta n_\alpha=n_\alpha^2-n_\alpha^1=0$. In this case, Eq. (2.25) gives the transverse displacement of the row α from $\mathbf{r}_1$ to $\mathbf{r}_2$ in terms of $\Delta\mathbf{h}$ and Δh_z. Long-range translational order is present if every row in the tiling has bounded transverse displacement.

The rows of set α divide a tiling into domains of constant n_α. In this respect a rhombus tiling can be viewed as a domain-wall system. The analogy is useful for understanding some physical properties of rhombus tilings, as we shall see in more detail in Sec. VI.

D. Square-gradient phason free energy

The phason correlation functions and Fourier properties of the rhombus-tiling system can be calculated if one assumes that long-wavelength phason fluctuations are governed by a square-gradient free energy. The general expression for such a free energy in systems with pentagonal symmetry has been discussed by Bak,[36] and by Levine *et al.*[33] In our case, it takes the form

$$\beta F=\beta F_0+\int d\mathbf{r}\left[\frac{K}{2}[(\nabla\bar{h}_1)^2+(\nabla\bar{h}_2)^2]+\frac{K_z}{2}(\nabla\bar{h}_z)^2\right]+K'\int d\mathbf{r}\nabla\bar{h}_1\times\nabla\bar{h}_2 , \quad (2.26)$$

where $\beta=1/k_BT$, $\bar{\mathbf{h}}=(\bar{h}_1,\bar{h}_2)$ and $\bar{h}_z$ are coarse-grained perpendicular-space coordinates, and K, K', and K_z are the corresponding phason elastic constants. Using

$$\nabla\bar{h}_1\times\nabla\bar{h}_2=\nabla\times(\bar{h}_1\nabla\bar{h}_2)$$

and the Stokes theorem, the last term in (2.26) can be transformed to a line integral along the system boundary, so that it remains constant if periodic or "fixed tile" boundary conditions are assumed. We shall ignore this term in the following discussion.

Using (2.26) the height-height correlation function at large distances can be calculated in a standard way, employing momentum-space diagonalization. Write

$$\begin{aligned}\mathbf{h}(\mathbf{r})&=\bar{\mathbf{h}}(\mathbf{r})+\delta\mathbf{h}(\mathbf{r}) ,\\ h_z(\mathbf{r})&=\bar{h}_z(\mathbf{r})+\delta h_z(\mathbf{r}) ,\end{aligned} \quad (2.27)$$

and assume that $\delta\mathbf{h}(\mathbf{r})$ and $\delta h_z(\mathbf{r})$, which denote deviations from the coarse-grained quantities, are bounded, we obtain

$$\begin{aligned}\langle[h_j(\mathbf{r})-h_j(0)][h_k(\mathbf{r})-h_k(0)]\rangle&\cong\langle[\bar{h}_j(\mathbf{r})-\bar{h}_j(0)][\bar{h}_k(\mathbf{r})-\bar{h}_k(0)]\rangle\\&=\frac{1}{2\pi^2K}\int_{-\pi/a}^{+\pi/a}dq_1\int_{-\pi/a}^{+\pi/a}dq_2\frac{1-\cos(\mathbf{q}\cdot\mathbf{r})}{|\mathbf{q}|^2}\delta_{jk}\\&=\frac{1}{\pi K}\delta_{jk}\ln\frac{|\mathbf{r}|}{a}+\text{const} ,\end{aligned} \quad (2.28)$$

and

$$\langle[h_z(\mathbf{r})-h_z(0)]^2\rangle\simeq\langle[\bar{h}_z(\mathbf{r})-\bar{h}_z(0)]^2\rangle=\frac{1}{\pi K_z}\ln\frac{|\mathbf{r}|}{a}+\text{const} , \quad (2.29)$$

where the angular brackets denote ensemble average and δ_{jk} is the Kronecker symbol.

The same method can be applied to calculate the average phonon fluctuations of a finite system under proper boundary conditions. The results are given by

$$\begin{aligned}\left\langle\frac{1}{N}\sum_{\mathbf{r}}\left|\mathbf{h}(\mathbf{r})-\frac{1}{N}\sum_{\mathbf{r}'}\mathbf{h}(\mathbf{r}')\right|^2\right\rangle&\simeq\frac{1}{2\pi^2K}\int_{CN^{-1/2}\le|\mathbf{q}|\le\pi/a}\frac{d\mathbf{q}}{|\mathbf{q}|^2}\\&=\frac{1}{2\pi K}\ln N+\text{const} ,\end{aligned} \quad (2.30)$$

and

$$\begin{aligned}\left\langle\frac{1}{N}\sum_{\mathbf{r}}\left|h_z(\mathbf{r})-\frac{1}{N}\sum_{\mathbf{r}'}h_z(\mathbf{r}')\right|^2\right\rangle&\simeq\frac{1}{4\pi^2K_z}\int_{CN^{-1/2}\le|\mathbf{q}|\le\pi/a}\frac{d\mathbf{q}}{|\mathbf{q}|^2}\\&=\frac{1}{4\pi K_z}\ln N+\text{const} ,\end{aligned} \quad (2.31)$$

where C is a number which depends on the boundary geometry. The constant terms in Eqs. (2.30) and (2.31) vary for

different boundary conditions, but remain the same value under a linear scale change of the system size for sufficiently large N. The logarithmic divergence of (2.30) and (2.31) with increasing system size implies the deBruijn surface is rough.

We now consider the ensemble average of the Fourier intensity given by Eq. (2.24) for a finite system at $\mathbf{E}=0$ and $\mathbf{E}_z=0$. Using (2.27), we write

$$\langle I_N(\mathbf{Q}_P^{\parallel})\rangle = \left\langle \sum_{\mathbf{r}} \exp\{-i\mathbf{Q}_P^{\perp}\cdot[\bar{\mathbf{h}}(\mathbf{r})-\bar{\mathbf{h}}(\mathbf{0})]-iQ_{Pz}[\bar{h}_z(\mathbf{r})-\bar{h}_z(\mathbf{0})]\} \right.$$
$$\left. \times\exp\{-i\mathbf{Q}_P^{\perp}\cdot[\delta\mathbf{h}(\mathbf{r})-\delta\mathbf{h}(\mathbf{0})]-iQ_{Pz}[\delta h_z(\mathbf{r})-\delta h_z(\mathbf{0})]\}\right\rangle . \tag{2.32}$$

Assuming $\delta\mathbf{h}(\mathbf{r})$ and $\delta h_z(\mathbf{r})$ to be bounded, the second phase factor in the above equation is close to 1 at sufficiently small $\mathbf{Q}_P^{\perp}$ and Q_{Pz}, in which case it can be assumed to be independent of the first phase factor. In this case the ensemble average can be carried out in a standard way, which yields

$$\langle I_N(\mathbf{Q}_P^{\parallel})\rangle \sim \int d\mathbf{r}\frac{1}{|\mathbf{r}|^{\eta(\mathbf{Q}_P^{\perp},Q_{Pz})}}$$
$$\sim N^{1-\eta(\mathbf{Q}_P^{\perp},Q_{Pz})/2} , \tag{2.33}$$

where

$$\eta(\mathbf{Q}_P^{\perp},Q_{Pz})=\frac{1}{2\pi K}|\mathbf{Q}_P^{\perp}|^2+\frac{1}{2\pi K_z}|Q_{Pz}|^2 . \tag{2.34}$$

Equations (2.33) and (2.34) do not hold when there is a strong correlation between the two phase factors in (2.32). This is the case at large values of $\mathbf{Q}_P^{\perp}$ and Q_{Pz}. In particular, since $h_z(\mathbf{r})$ takes only integral values, adding an integer multiple of 2π to Q_{Pz} does not change the scattering intensity. Therefore,

$$\eta(\mathbf{Q}_P^{\perp},Q_{Pz}+2\pi)=\eta(\mathbf{Q}_P^{\perp},Q_{Pz}) . \tag{2.35}$$

Nevertheless, Eq. (2.34) may still give the correct Q_{Pz} dependence of η at $Q_{Pz}=0,\pm 2\pi/5$, and possibly at $Q_{Pz}=\pm 4\pi/5$. [Equation (2.35) reflects the fact that the indexing of diffraction peaks of tilings with $\mathbf{E}_z=0$ is nonunique with respect to adding a common integer to each of the five indices m_α.[27]]

The Fourier intensity for an *infinite* tiling at a scattering wave vector in the neighborhood of $\mathbf{Q}_P^{\parallel}$ is given by

$$I(\mathbf{Q}_P^{\parallel}+\delta\mathbf{q})\sim \int d\mathbf{r}\frac{e^{i\delta\mathbf{q}\cdot\mathbf{r}}}{|\mathbf{r}|^{\eta(\mathbf{Q}_P^{\perp},Q_{Pz})}}$$
$$\sim \frac{1}{|\delta\mathbf{q}|^{2-\eta(\mathbf{Q}_P^{\perp},Q_{Pz})}} , \tag{2.36}$$

thus it exhibits a power-law dependence (divergence) on $\delta\mathbf{q}$.

The logarithmic dependence of height-height correlations [Eqs. (2.28) and (2.29)], and algebraic diffraction peaks [Eq. (2.36)], are characteristic of 2D systems possessing *quasi-long-range* translational order.

For tilings with small phason strain, one expects the equations in this subsection to be approximately correct if $\mathbf{h}$ and h_z are replaced by $\tilde{\mathbf{h}}$ and $\tilde{h}_z$ [Eq. (2.21)], and $\mathbf{Q}_P^{\parallel}$ by $\mathbf{Q}_P^{\parallel}+\Delta\mathbf{Q}^{\parallel}$ [Eq. (2.18)]. Due to the absence of pentagonal symmetry in strained tilings, the elastic constant K in this case may assume a slightly different value for each of the two components of $\tilde{\mathbf{h}}$.

III. ZERO-TEMPERATURE PHASON ELASTICITY

Socolar *et al.* suggested that unit-cell models of the sort discussed in this paper may exhibit an unusual kind of phason elasticity at $T=0$, with a linear dependence of elastic energy on the strain.[17] In this section we present an analysis which yields a lower bound or, in special cases, an exact expression for the energy of uniformly strained tilings. Though our conclusion is the same as in Ref. 17, the discussion provides new insights into the problem, as well as some additional results.

A. Exact elastic energy for four-vertex tilings

A *four-vertex* tiling is a tiling whose h_z coordinates of vertices are restricted to four consecutive integers. It is the simplest case of the Penrose model with fluctuations along the commensurate h_z direction suppressed, but with *no* restriction on fluctuations in the incommensurate 2D perpendicular space $\mathbf{h}$. Without loss of generality, we shall take the four possible h_z values to be 1, 2, 3, and 4. Note that Penrose tilings, which constitute the ground state of models with energy (2.2), belong to this class.

The four-vertex tiling ensemble is simply a realization of the Penrose model at $\varepsilon_{DD}=\varepsilon_{SD}=\infty$, i.e., with no unmatched double arrows. To see this, we note that around four corners of a given rhombus, the set of h_z values is given by either (1,2,2,3), or (2,3,3,4). In either case it is possible to orient the rhombus such that the double arrows are on the edges linked to the $h_z=1$ or 4 vertex and point toward the vertex. By arranging every rhombus in the tiling this way, all double arrows are on the edges linked to vertices with $h_z=1$ or 4, and match one another in direction. The opposite is also true, i.e., any tiling with all double arrows matched in pairs is a four-vertex tiling.

The enumeration of $(SS)^-$ bonds in a four-vertex tiling can be done as follows. Consider first a row of set $\alpha=0$, which consists of tiles of type (0,1), (0,2), (3,0), and (4,0), as shown in Fig. 3(a). Along the row one sees an alternating sequence of SS and DD bonds between successive cells.

Figure 3(b) shows six basic cell-and-bond configurations in between two successive DD bonds in the row. We find that combinations of a tile of type (0,1) or (3,0) with another tile of type (0,2) or (4,0) give rise to an $(SS)^+$ bond (C_1, C_2, and C_3), while other combinations

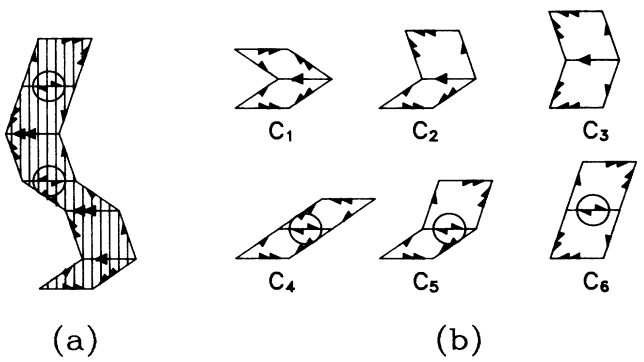

FIG. 3. (a) A row of tiles with common edges along $\hat{\mathbf{e}}_0^{\parallel}$ direction. *SS* and *DD* bonds alternate along the row. Unmatched single arrow pairs are indicated by the circles. (b) Six non-symmetry-related two-tile configurations, each containing an *SS* bond in the middle. $(SS)^-$ bonds are found in C_4, C_5, and C_6.

give rise to an $(SS)^-$ bond (C_4, C_5, and C_6). Thus, a *lower bound* for the number of $(SS)^-$ bonds in rows of set 0 is given by the excess number of (0,1) and (3,0) type rhombuses with respect to that of (0,2) and (4,0) type,

$$\Delta N_{\alpha=0} = A|\rho_{(0,1)}+\rho_{(3,0)}-\rho_{(0,2)}-\rho_{(4,0)}|/2 , \tag{3.1}$$

where A is the area of the tiling. The factor 2 in (3.1) accounts for the fact that it takes two excess (0,1) or (3,0) rhombuses to make an $(SS)^-$ bond.

Equation (3.1) can be generalized to rows running in other directions in an obvious way. Summing over all five sets of rows gives a lower bound for the elastic energy per unit area

$$\epsilon_{SS}\sum_{\alpha=0}^{4}\Delta N_\alpha/A=\frac{4\epsilon_{SS}}{5\sqrt{5}a^2}\sum_{\alpha=0}^{4}|\hat{\mathbf{e}}_\alpha^{\parallel}\times\mathbf{E}^T\hat{\mathbf{e}}_\alpha^{\perp}| , \tag{3.2}$$

where we have used Eq. (2.14) at $\mathbf{E}_z=0$. From (3.2) and (2.15) we obtain a lower bound for the elastic energy *per tile*

$$e^{(-)}(\mathbf{E},\mathbf{E}_z=\mathbf{0})=\frac{4\epsilon_{SS}}{5\sqrt{5}a^2\rho_T}\sum_{\alpha=0}^{4}|\hat{\mathbf{e}}_\alpha^{\parallel}\times\mathbf{E}^T\hat{\mathbf{e}}_\alpha^{\perp}| . \tag{3.3}$$

Here

$$\rho_T=\rho_F+\rho_S=\frac{4\tau}{5a^2}(1-\tau^{-3}\det\mathbf{E})\sin\frac{2\pi}{5} . \tag{3.4}$$

In the Appendix we consider a special class of four-vertex tilings whose energy per tile can be calculated exactly. The result coincides with (3.3), which establishes (3.3) as the *exact* elastic energy for four-vertex tilings at $T=0$.

An interesting, perhaps artificial feature of the Penrose model is that there is no lock-in term in the energy (3.3) at strains corresponding to periodic tilings, in contrast to the typical behavior of other incommensurately modulated systems. It is plausible that the degeneracy among different periodic tilings at a given strain, which is the origin of above-mentioned behavior, disappears when sufficiently long-range interactions among the vertices (or tiles) are introduced, or when the tiles are allowed to deform in response to a softened atomic potential.

B. A general lower bound for the strain energy

We now turn to the general class of rhombus tilings with energy (2.2). To obtain a lower bound for the elastic energy associated with $\mathbf{E}_z$, we apply a similar counting scheme as in the previous case.

For the following discussion it is convenient to introduce an h_z^0 coordinate for every cell. Let $\mathbf{r}$ be the corner of a decorated tile to which two double arrows point. The h_z^0 coordinate of the tile equals $h_z(\mathbf{r})-4$ if the two double arrows are along the $\hat{\mathbf{e}}_\alpha^{\parallel}$ directions, and $h_z(\mathbf{r})-1$ otherwise. Unlike h_z, h_z^0 depends on both the vertex position and arrow configuration. In the special case of four-vertex tiling, all cells have the same h_z^0 coordinate.

As before, we first consider a finite segment of a row of set $\alpha=0$, which contains $(DD)^-$ and *SD* bonds. Such a row consists of "domains" of constant h_z^0 separated by "walls." Each wall is a $(DD)^-$ bond [Fig. 4(a)] or an *SD* bond [Fig. 4(b)]. The heavy plain line in Fig. 4(b) designates an edge which is decorated with a single arrow (not shown) pointing in either the $\hat{\mathbf{e}}_0^{\parallel}$ or the $-\hat{\mathbf{e}}_0^{\parallel}$ direction, as the case may be. An *SD* bond shift h_z^0 by 1, while a *DD* bond shifts it by 2. Let A and B be two vertices at the two ends of the segment and on the same side of the row, and $\Gamma_{DD}(0)$ and $\Gamma_{SD}(0)$ be the number of $(DD)^-$ and *SD* bonds in the segment, respectively. Then

$$2\Gamma_{DD}(0)+\Gamma_{SD}(0)\geq|\Delta h_z^0|\simeq|\Delta n_1+\Delta n_2+\Delta n_3+\Delta n_4| , \tag{3.5}$$

where $\Delta n_\alpha=n_\alpha^B-n_\alpha^A$. Note that Δn_1, Δn_2, $-\Delta n_3$, and $-\Delta n_4$ give the number of (0,1), (0,2), (3,0), and (4,0) type rhombuses in the segment, respectively.

Let $\gamma_{SS}(\alpha)$, $\gamma_{DD}(\alpha)$, and $\gamma_{SD}(\alpha)$ be the number of $(SS)^-$, $(DD)^-$, and *SD* bonds in rows of set α per unit area. From Eqs. (3.5) and (2.14) we obtain (for general α)

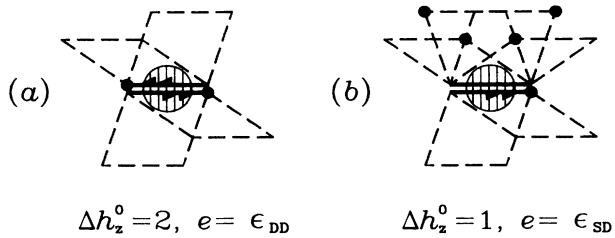

FIG. 4. (a) A $(DD)^-$ bond, $\Delta h_z^0=2$. Solid circles indicate vertices to which double arrows of the corresponding rhombus point. (b) An *SD* bond ("+" or "−"), $\Delta h_z^0=1$. The top solid line is decorated with a single arrow, pointing in either direction.

$$2\gamma_{DD}(\alpha)+\gamma_{SD}(\alpha)\geq|\rho_{(\alpha,\alpha+1)}+\rho_{(\alpha,\alpha+2)}-\rho_{(\alpha-2,\alpha)}-\rho_{(\alpha-1,\alpha)}|$$
$$=\frac{2}{5a^2}|\hat{\mathbf{e}}_\alpha^{\parallel}\times\mathbf{E}_z^T+(\mathbf{E}^T\hat{\mathbf{e}}_\alpha^{\perp})\times\mathbf{E}_z^T| \ . \quad (3.6)$$

One can combine this result with (3.1) to give a general lower bond for the elastic energy. To obtain the constraint on $\gamma_{SS}(\alpha)$, we note that while the discussion leading to (3.1) still holds in the presence of $(DD)^-$ bonds, each SD bond introduces an additional tile, which alters the succession of single and double arrow bonds along the row. Thus, (3.1) should be replaced with

$$2\gamma_{SS}(\alpha)+\gamma_{SD}(\alpha)\geq|\rho_{(\alpha,\alpha+1)}-\rho_{(\alpha,\alpha+2)}+\rho_{(\alpha-2,\alpha)}-\rho_{(\alpha-1,\alpha)}|$$
$$=\frac{4}{5\sqrt{5}a^2}|\hat{\mathbf{e}}_\alpha^{\parallel}\times\mathbf{E}^T\hat{\mathbf{e}}_\alpha^{\perp}+\tfrac{1}{4}\hat{\mathbf{e}}_\alpha^{\parallel}\times\mathbf{E}_z^T+\tfrac{1}{4}\mathbf{E}_z^T\times\mathbf{E}^T\hat{\mathbf{e}}_\alpha^{\perp}| \ . \quad (3.7)$$

Summing over contributions from all five rows, and minimizing the energy separately for each row, we obtain a general lower bound for the elastic energy per tile

$$e^{(-)}(\mathbf{E},\mathbf{E}_z)=\rho_T^{-1}\sum_{\alpha=0}^{4}\min_{\gamma_{SS}(\alpha),\gamma_{DD}(\alpha),\gamma_{SD}(\alpha)}\times[\gamma_{SS}(\alpha)\varepsilon_{SS}+\gamma_{DD}(\alpha)\varepsilon_{DD}+\gamma_{SD}(\alpha)\varepsilon_{SD}] \ , \quad (3.8)$$

subjected to the constraints (3.6), (3.7), and

$$\gamma_{SS}(\alpha)\geq 0, \quad \gamma_{DD}(\alpha)\geq 0, \quad \gamma_{SD}(\alpha)\geq 0 \ . \quad (3.9)$$

The expression in (3.8) can be evaluated at any given strain using the standard methods in linear programming.[37] At small strain, the constraints (3.6) and (3.7) are dominated by terms linear in $\mathbf{E}$ and $\mathbf{E}_z$. Thus, if one multiplies both $\mathbf{E}$ and $\mathbf{E}_z$ by a given factor, the lower bound (3.8) changes by the same factor.

IV. THERMAL ROUGHENING

In this section we examine a heuristic argument which suggests that thermal roughening of the deBruijn surface occurs at all $T>0$. We shall start by reconsidering the $T=0$ case, and focus on the energy associated with a "step" on an otherwise flat deBruijn surface.

A key notion in the following discussion is "worm," defined as an *unbroken* sequence of three tile hexagons, as shown in Fig. 5. The length of a worm is defined to be the number of hexagons in the string. The two sides of each hexagon in a worm are symmetrically decorated with arrows, thus flipping one or more hexagons [shown by the shaded portion in Fig. 5(b)] in the worm does not create (or destroy) unmatched arrow pairs on the two sides of the worm. Note that arbitrarily long worms can be found in a Penrose tiling. Different Penrose tilings can be brought to one another through a succession of flips of worms which run across the system.

Consider a configuration obtained by properly joining two Penrose tilings which have slightly different average $\mathbf{h}$ coordinates, as illustrated in Fig. 6. This is analogous to constructing a step on the surface of a crystal. The interface of the two parts is indicated by the dashed line. The Penrose tiling on the right coincides with the continuation of the Penrose tiling on the left, except at a set of worms (shaded). Unmatched single arrows, indicated by the dots, appear in partially flipped worms which run across the interface (heavy line). The density of unmatched arrows along the interface is inversely proportional to the typical length scale l of the network of flipped worms, which can be estimated as follows.

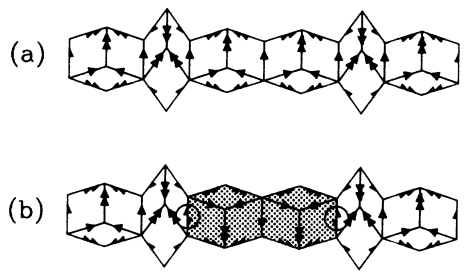

FIG. 5. (a) A worm formed by six hexagons. Edges on the two sides of the worm are decorated symmetrically. (b) The same worm with two hexagons (shaded) flipped. As a result, two $(SS)^-$ bonds, indicated by circles, are created.

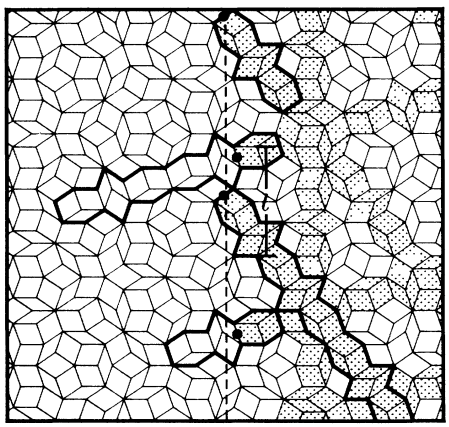

FIG. 6. Two Penrose tilings joined along the dashed line. The shaded tiles on the right-hand side must be rearranged if we are to continue the left Penrose tiling across the dashed line. Solid circles indicate $(SS)^-$ bonds. Worms running across the dashed line are indicated by the heavy lines. The typical interspacing of the network of flipped worms is l.

Suppose that the difference in average $\mathbf{h}$ between the two tilings is $\Delta\bar{\mathbf{h}}$. Contribution to this difference comes only from vertices which lie in the flipped worms. Noting that a typical cell of the network of flipped worms contains l^2 vertices surrounded by l flipped hexagons, we obtain

$$|\Delta\bar{\mathbf{h}}| \sim l^{-1} . \tag{4.1}$$

The energy of the interface per unit length is given by

$$\varepsilon_{SS} l^{-1} \sim \varepsilon_{SS} |\Delta\bar{\mathbf{h}}| , \tag{4.2}$$

from which the $T=0$ linear elastic energy can be rederived.

The behavior (4.2) is typical for a solid-gas interface below its roughening temperature, though there the height shift is usually only discrete. The usual argument for the thermal roughening of such an interface assumes a finite entropy $k_B \ln a > 0$ for a step of unit length. The free energy of a step of length L is thus given by

$$f(L) \simeq L e_0 - L k_B T \ln a , \tag{4.3}$$

which vanishes at $T_R \simeq e_0/(k_B \ln a)$. Here e_0 is the energy of the step per unit length. For $T > T_R$ the interface becomes rough and steps can no longer be unambiguously identified.

Let us now consider a similar argument applied to the deBruijn surface. Inspecting Fig. 6, we see that each $(SS)^-$ bond (shown by a solid dot) can be moved independently to any other shared edge of two hexagons in the same worm (shown by the region enclosed by heavy lines) through successive hexagon flips. Since there are no new $(SS)^-$ bonds created in the process, all configurations thus obtained are degenerate. From this observation we obtain an estimate for the entropy of a step of length L and shift $\Delta\bar{\mathbf{h}}$,

$$s(L) \simeq k_B \ln l^{L/l} \simeq -L k_B |\Delta\bar{\mathbf{h}}| \ln |\Delta\bar{\mathbf{h}}| , \tag{4.4}$$

where we used (4.1). Combining (4.4) with (4.2) gives the free energy of the step,

$$\begin{aligned} f(L) &= \varepsilon_{SS} L/l - T s(L) \\ &\simeq L |\Delta\bar{\mathbf{h}}| (\varepsilon_{SS} + k_B T \ln |\Delta\bar{\mathbf{h}}|) . \end{aligned} \tag{4.5}$$

Thus, at any given $T > 0$, $f(L)$ can be made to vanish for sufficiently small $\Delta\bar{\mathbf{h}}$. This gives the argument for the roughening of the deBruijn surface at any $T > 0$.

One should keep in mind that, though the estimate for the *minimum* number of unmatched single arrows, (4.2), is correct independent of temperature, at $T > 0$ there will be an additional number of thermally excited ones which tend to reduce both the *excess* number of unmatched single arrows due to the step, and the estimate for its entropy, (4.4). Thus, strictly speaking, the above argument applies only at $T=0$. A rigorous analysis of the step free energy at $T > 0$ lies outside the scope of the present paper.

V. INFLATION TRANSFORMATION

A Penrose tiling has the interesting property that, by suitably selecting a subset of vertices and connecting them with bonds of length τ times the bond length of the original tiling, one obtains another rhombus tiling which again satisfies the matching rules. This is known as the *inflation* symmetry of the Penrose tilings.[8,24–27]

In this section we generalize the inflation transformation to tilings which contain a small number of unmatched single arrows. The scheme provides a natural framework for a real-space renormalization-group analysis on the four-vertex tiling model. We show that the equilibrium distribution in the quasicrystal phase at arbitrarily small $T > 0$ flows under successive RG transformations toward the infinite-temperature random-tiling limit. The analysis provides another compelling argument for the thermal roughening of the deBruijn surface at all $T > 0$. In the last part of the section we discuss the crossover behavior of the elastic energy as the phason strain is increased.

A. Inflation of a rhombus tiling

For simplicity, we shall limit the discussion to four-vertex tilings. The h_z coordinates for the vertices are assumed to be from 1 to 4. Such a tiling can be alternatively viewed as a tiling by queens, kings, and stars, as shown in Fig. 7. The center vertices of the three types of cells have $h_z = 1$ or 4.

The procedure for performing inflation transformation is illustrated in Fig. 8, which consists of two steps: (i) Construct a tiling by queens, kings, and stars [Fig. 8(b)] from the original tiling χ [Fig. 8(a)]. (ii) Add a center vertex to each queen, king, and star to obtain an inflated rhombus tiling $\tilde{\chi}$ [Fig. 8(c)], which is again a four-vertex tiling. Each tile in $\tilde{\chi}$ can be decorated with arrows according to Fig. 7.

Specifically, we first find all vertices of χ whose $h_z = 1$ or 4 [marked by open circles in Fig. 8(b)] and connect them with bonds of length τa, where a is the bond length of χ. The result is a tiling of queens, kings, and stars if there is a sufficiently large distance (two or more tiles) between every pair of $(SS)^-$ bonds in χ. Additional cell shapes can rise at places where two or more $(SS)^-$ bonds are placed next to each other. If the overall density of unmatched arrows is low, such "bad" cells do not appear often, and when they do, they are usually surrounded by the "good" ones, and can be removed by shifting the position of one or two vertices around each bad cell. In the example shown in Fig. 8(b), the bad cell is removed by moving the vertex A to A', and reconnecting it to the neighboring vertices, as indicated by the dashed lines.

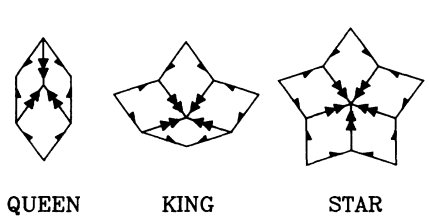

FIG. 7. Queen, king, and star, corresponding to three, four, and five incoming DD bonds at the center vertex, respectively.

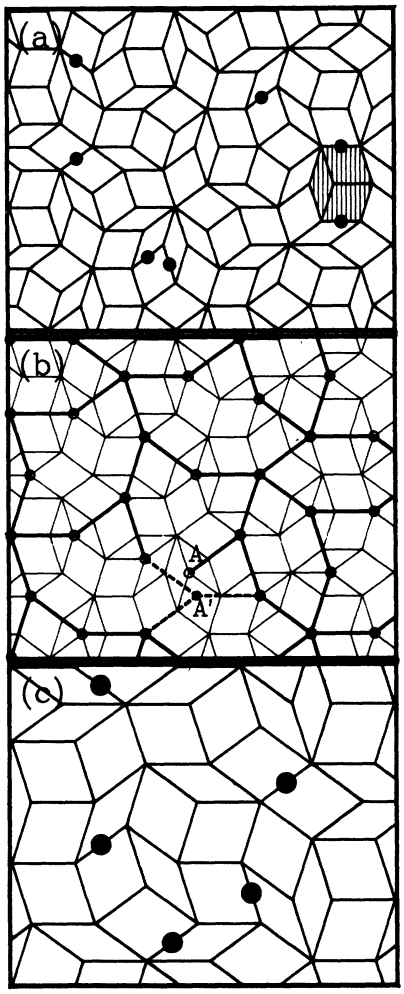

FIG. 8. Inflation transformation: (a) a four-vertex tiling χ, (b) a tiling of queens, kings, and stars, shown by the heavy lines, obtained by connecting vertices of χ whose h_z coordinate equals 1 or 4, and (c) the inflated tiling $\tilde{\chi}$. Solid circles indicate $(SS)^-$ bonds. The shaded long hexagon in (a) illustrates a short-wavelength fluctuation which is integrated out in the inflation.

In the second step, we first add a center vertex to every king and star, for which there is a unique choice for its position. The situation is different for the queens, where the following rule is used: If the two possible choices for the position of the center vertex at a given cell give rise to different number of unmatched single arrows, pick the one which corresponds to a smaller number of unmatched arrows in $\tilde{\chi}$; otherwise, pick either of the two with equal probability $\frac{1}{2}$. In the case when the choice for one queen-shaped cell affects the choice for another (which rarely occurs at small density of unmatched single arrows), we apply the above rule one at a time, following a random selection of queen-shaped cells.

For a Penrose tiling the above scheme coincides with the standard inflation rules, and generates a unique inflated tiling. In general, we expect the transformation to be a many-to-many mapping: different tilings χ can be mapped to the same inflated tiling $\tilde{\chi}$, while a given χ may correspond to more than one $\tilde{\chi}$. Note that flipping a hexagon of the type shown by the crosshatched tiles in Fig. 8(a) does not change $\tilde{\chi}$. In a vague sense, such flips represent the type of local phason fluctuations which are integrated out under the inflation transformation.

The 5D coordinates $\{\tilde{n}_\alpha\}$ for the vertices of the inflated tiling can be obtained using the standard procedure discussed in Sec. II B. For convenience, we choose the origin of $\tilde{\chi}$ to be at the same position as that of χ, and let $\tilde{h}_z=\sum_\alpha \tilde{n}_\alpha$ to be from 1 to 4. At the common vertices of χ and $\tilde{\chi}$ (those with $h_z=1$ or 4), we have

$$\tilde{n}_\alpha=\begin{cases} n_{\alpha-1}+n_{\alpha+1} & \text{for } h_z=1,\tilde{h}_z=2\ , \\ n_{\alpha-1}+n_{\alpha+1}-5 & \text{for } h_z=4,\tilde{h}_z=3\ . \end{cases} \tag{5.1}$$

The perpendicular space coordinates $\tilde{\mathbf{h}}$ for these vertices are related by

$$\tilde{\mathbf{h}}(\tilde{\mathbf{r}})\equiv\sum_\alpha \tilde{n}_\alpha \hat{\mathbf{e}}_\alpha^\perp=\sum_\alpha (n_{\alpha-1}+n_{\alpha+1})\hat{\mathbf{e}}_\alpha^\perp=-\tau\mathbf{h}(\mathbf{r})\ . \tag{5.2}$$

Thus, long-wavelength phason fluctuations in χ remain in $\tilde{\chi}$. Its amplitude is enhanced by a factor of τ.

Noting that the bond length of $\tilde{\chi}$ is τ times that of χ, we obtain from Eqs. (2.11) and (5.2),

$$\tilde{\mathbf{E}}=-\tau^2\mathbf{E}\ . \tag{5.3}$$

Equation (5.3) holds not only for the average strain of entire system, but also in a suitable coarse-grained local sense. Thus, the relation tells us that a random (rough) tiling becomes even more random (rough) under the inflation transformation.

B. Fugacity renormalization

The partition function of the four-vertex tiling model can be expressed as

$$Z(\beta,N)=\sum_\chi \exp[-\beta E(\chi)]=\sum_\chi \prod_i^{M(\chi)} z_i\ , \tag{5.4}$$

where N is the total number of tiles, $\beta=1/k_BT$, $E(\chi)$ is the energy (2.2), $M(\chi)$ is the number of $(SS)^-$ bonds in χ, and $z_i=\exp(-\beta\varepsilon_{SS})$ is the Boltzmann weight (fugacity) of the ith $(SS)^-$ bond. The sum is over all possible tiling configurations consistent with a given boundary condition.

Adopting the standard renormalization procedure, we write

$$Z(\beta,N)=Z_0(\beta,N)\tilde{Z}(\tilde{\beta},\tilde{N})\ , \tag{5.5}$$

where

$$\tilde{Z}(\tilde{\beta},\tilde{N})=\sum_{\tilde{\chi}} \exp[-\tilde{\beta}\tilde{E}(\tilde{\chi})] \tag{5.6}$$

is the partition function of the inflated tiling with $\tilde{N}$ tiles, and $Z_0(\beta,N)$ gives the contribution to Z due to the degrees of freedom which are summed over in the inflation process. The renormalized energy $\tilde{E}(\tilde{\chi})$ is defined such that

$$\exp[-\tilde{\beta}\tilde{E}(\tilde{\chi})]=\sum_{\chi\to\tilde{\chi}} \exp[-\beta E(\chi)]/Z_0(\beta,N)\ , \tag{5.7}$$

where the sum is over all possible configurations χ which

are mapped to $\tilde{\chi}$ under the inflation transformation.

At low density of $(SS)^-$ bonds, it makes sense to write (5.7) as a product of fugacities for the $(SS)^-$ bonds $\tilde{z}_i$,

$$\exp[-\tilde{\beta}\tilde{E}(\tilde{\chi})]=\prod_i \tilde{z}_i \ . \tag{5.8}$$

In the following we derive a renormalization equation for $\tilde{z}_i$, assuming that the $(SS)^-$ bond is contained in a worm, which is the case if the bond is sufficiently far apart from other $(SS)^-$ bonds.

Consider a worm which contains certain number of $(SS)^-$ bonds, as shown in Fig. 9(a). If we divide the worm into a number of sections according to the arrangement of the short hexagons (queens), in the way shown in the figure, the inflation transformation can be carried out for each section, independent of its neighboring sections. At low density of $(SS)^-$ bonds, each such section contains one or two long hexagons (two fat tiles and one skinny tile).

Figures 9(b)–9(d) give a list of possible configurations for sections which contain one $(SS)^-$ bond, along with bonds of $\tilde{\chi}$ (shown by the heavy lines) determined by the local configuration. Two Boltzmann weights are needed for our purpose: z_1 for an $(SS)^-$ bond between a fat and a skinny tile (see C_5 in Fig. 3), and z_2 for an $(SS)^-$ bond between two fat tiles (C_6 in Fig. 3).

In Fig. 9(b), two different configurations of the section, each of which contains a z_1-type $(SS)^-$ bond, lead to the same set of bonds in $\tilde{\chi}$, including a $\tilde{z}_2$-type $(SS)^-$ bond. Thus, we have

$$\tilde{z}_2=2z_1 \ . \tag{5.9}$$

Figure 9(c) illustrates a segment of two long hexagons containing a z_1-type $(SS)^-$ bond, which gives a unique $\tilde{z}_1$-type $(SS)^-$ bond in the inflated pattern. The segment shown in Fig. 9(d), on the other hand, corresponds to two different $\tilde{z}_1$-type inflated local patterns, each assigned a probability $\frac{1}{2}$. Thus, we write

$$\tilde{z}_1=z_1+\tfrac{1}{2}z_2 \tag{5.10}$$

for the fugacity of the $(SS)^-$ bond in the inflated pattern of Fig. 9(c) and the left-hand side of Fig. 9(d). [We note that since the fugacity of an $(SS)^+$ bond in $\tilde{\chi}$ is $1+O(z_1^2)$, Eqs. (5.9) and (5.10) should contain a second order correction if (5.8) is assumed. However, at low temperatures $z_1 \ll 1$, so that this second order term can be safely ignored.]

Rewriting Eqs. (5.9) and (5.10) in a matrix form, we obtain

$$\begin{bmatrix}\tilde{z}_1\\ \tilde{z}_2\end{bmatrix}=\begin{bmatrix}1 & \frac{1}{2}\\ 2 & 0\end{bmatrix}\begin{bmatrix}z_1\\ z_2\end{bmatrix}=M\begin{bmatrix}z_1\\ z_2\end{bmatrix} \ . \tag{5.11}$$

The eigenvalues of the matrix M are given by τ and $-1/\tau$. Since z_1, z_2, and M are all positive, the transformation carries z_1 and z_2 toward larger values with an asymptotic growth rate τ.

Equations (5.9) and (5.10) may not hold for $(SS)^-$ bonds which occur at the end or outside of a worm. Since the percentage of such $(SS)^-$ bonds in equilibrium configurations at low temperatures is very small, we expect that the renormalization of the equilibrium distribution is controlled by the behavior of z_1 and z_2.

C. Renormalization-group flow and elastic energy

Writing approximately $\tilde{z}_i \simeq z_i^0 \exp(-\tilde{\beta}\varepsilon_{SS})$ with $\tilde{\beta}=1/k_B\tilde{T}$, Eq. (5.11) can be replaced with, after a sufficient number of iterations,

$$\tilde{\beta}\simeq\beta-\ln\tau/\varepsilon_{SS} \ . \tag{5.12}$$

The RG flow on the T-E plane, as defined by (5.3) and (5.12), is shown schematically in Fig. 10. The right ($T=\infty$) and upper ($|\mathbf{E}|\simeq 1$) boundaries of the box are limits on the validity of the RG equations. The origin O, representing the $T=0$ Penrose tilings, is the only fixed point of the transformation, and is unstable. The dashed line, given by $|\mathbf{E}|\simeq\exp(-2\varepsilon_{SS}/k_BT)$, separates two re-

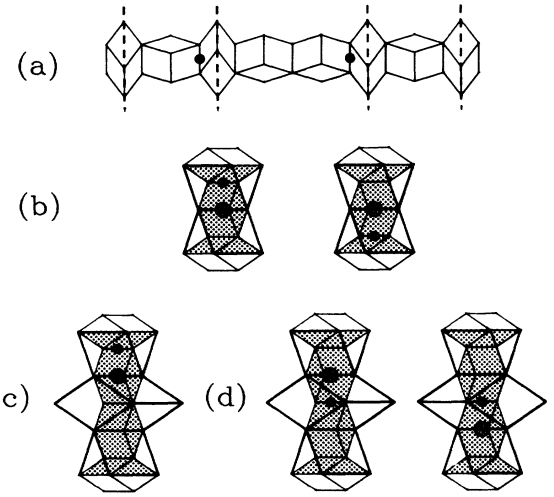

FIG. 9. (a) Dividing a worm into sections according to the arrangement of short hexagons. (b) Two possible configurations for sections containing one long hexagon and an $(SS)^-$ bond, along with bonds of the inflated pattern, as shown by the heavy lines. (c) A two-long-hexagon pattern containing an $(SS)^-$ bond which gives a unique inflated pattern. (d) Another two-long-hexagon pattern containing an $(SS)^-$ bond which gives two different inflated patterns, each assigned a probability $\frac{1}{2}$.

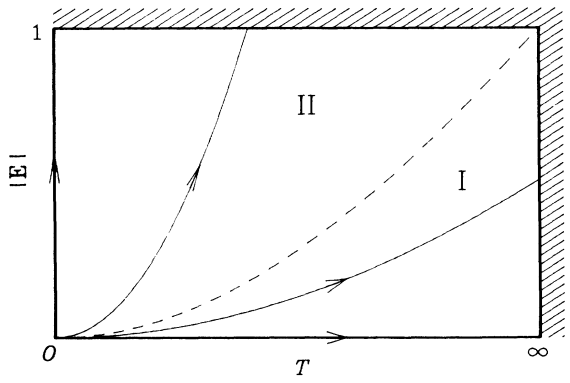

FIG. 10. Schematic plot of the renormalization-group flow on the T-E plane.

gions I and II. Points in region I flow to the infinite-temperature limit. These include the entire quasicrystal phase at $T>0$, represented by the lower boundary of the box. Points in region II flow to the large strain limit.

In the following we show that the elastic (free) energy is quadratic in the phason strain $\mathbf{E}$ in region I, but becomes linear in region II. Consider the reduced free energy per tile

$$\phi(\beta,\mathbf{E})=-\lim_{N\to\infty}\frac{1}{N}\ln Z(\beta,N)\simeq\phi_0(\beta,\mathbf{E})+\tau^{-2}\phi(\tilde{\beta},\tilde{\mathbf{E}}) , \tag{5.13}$$

where

$$\phi_0(\beta,\mathbf{E})=-\lim_{N\to\infty}\frac{1}{N}\ln Z_0(\beta,N) , \tag{5.14}$$

and the limits are taken at fixed $\mathbf{E}$. The factor τ^{-2} in front of the last term in (5.13) accounts approximately for the reduction of the number of tiles in the inflated system.

The factor Z_0 includes contributions to the partition function from flips of long hexagons mentioned previously. In a perfect Penrose tiling, the number of such hexagons is $\tau^{-2}N$. We expect this to be approximately true at low temperatures, too. Each such hexagon contributes (approximately independently) a factor $1+z_1^2$ or $1+z_1z_2$ to Z_0. Hence, we obtain

$$\phi_0(\beta,\mathbf{E})\simeq-\tau^{-2}Ae^{-2\beta\varepsilon_{SS}} , \tag{5.15}$$

where we have used $z_1\sim z_2\sim\exp(-\beta\varepsilon_{SS})$. Here A is some constant which depends on the ratio of z_1 and z_2.

Using (5.15), Eq. (5.13) can be iterated n times to give

$$\phi(\beta,\mathbf{E})\simeq-A\tau^{-2}ne^{-2\beta\varepsilon_{SS}}+\tau^{-2n}\phi(\beta-n\ln\tau/\varepsilon_{SS},\tau^{2n}\mathbf{E}) , \tag{5.16}$$

where we have used Eqs. (5.3) and (5.12), and the inversion symmetry $\phi(\beta,\mathbf{E})=\phi(\beta,-\mathbf{E})$.

Starting from a point $(T,\mathbf{E})$ below the dashed line in Fig. 10, i.e., $|\mathbf{E}|e^{2\beta\varepsilon_{SS}}<1$, one arrives at the right boundary of the box after $n\simeq\beta\varepsilon_{SS}/\ln\tau$ transformations. Assuming that the reduced free energy at infinite temperature depends quadratically on the phason strain, we get from (5.16)

$$\phi(\beta,\mathbf{E})\simeq-\frac{A}{\tau^2\ln\tau}\beta\varepsilon_{SS}e^{-2\beta\varepsilon_{SS}}+Be^{-2\beta\varepsilon_{SS}}+\tfrac{1}{2}K(\beta)|\mathbf{E}|^2 , \tag{5.17}$$

where B is the entropy of the infinite temperature random tiling, and

$$K(\beta)=K_\infty e^{2\beta\varepsilon_{SS}} \tag{5.18}$$

is the phason elastic constant, whose value at $T=\infty$ is given by K_∞.

For $|\mathbf{E}|e^{2\beta\varepsilon_{SS}}>1$, one arrives at the upper boundary of the box after $n\simeq-\frac{1}{2}\ln|\mathbf{E}|/\ln\tau$ iterations. Equation (5.16) then yields

$$\phi(\beta,\mathbf{E})\simeq\frac{A}{2\tau^2\ln\tau}e^{-2\beta\varepsilon_{SS}}\ln|\mathbf{E}|+|\mathbf{E}|\phi(\beta-n\ln\tau/\varepsilon_{SS},\tau^{2n}\mathbf{E}) . \tag{5.19}$$

At fixed phason strain $\mathbf{E}$, the first term vanishes as $T\to0$, while the second term reduces to the zero-temperature linear elastic energy (3.3).

Figure 11 is a schematic plot of the energy per tile $e=\partial\phi/\partial\beta$ (same as the number of unmatched single arrows per tile multiplied by ε_{SS}) against $\mathbf{E}$ at $T=0$ and $T>0$. For $T>0$ the excess number of unmatched single arrows increases quadratically with $\mathbf{E}$ for small $\mathbf{E}$, but changes to a linear behavior at $|\mathbf{E}|>e^{-2\beta\varepsilon_{SS}}$.

The quadratic form (5.17) at small $\mathbf{E}$ governs thermal fluctuations of phasons of sufficiently long wavelength, and leads to the roughening of the deBruijn surface at arbitrarily low temperatures. This conclusion agrees with the heuristic argument presented in the previous section.

VI. MONTE CARLO SIMULATION OF RHOMBUS-TILING MODELS

A. Method

Due to lack of exact results, Monte Carlo simulations provide a valuable source of information to the equilibrium properties of our model. There are some technical issues involved in applying the standard method to rhombus-tiling systems. Since there has not been a detailed account of the approach in the literature, in this section and in Sec. VI B we discuss in some detail the algorithm used in studying the four-vertex, binary random, and "unconstrained" random tilings. The last case is defined to be the infinite-temperature limit of the Penrose model at finite ε_{SS}, ε_{SD}, and ε_{DD}.

The algorithm is based on the Metropolis importance sampling scheme. Transition from one tiling to another is done through a sequence of "flips" of a few prescribed local clusters of tiles, which we take to be long and short hexagons [Fig. 12(a)] except for the binary tilings, where an octagon is taken instead [Fig. 12(b)]. Each hexagon or octagon is uniquely identified by a vertex, as indicated by the solid circles in Fig. 12.

In the case of hexagon flips, the basic Monte Carlo move consists of two steps: (i) randomly select a vertex in the system; (ii) if the vertex represents a hexagon, flip the

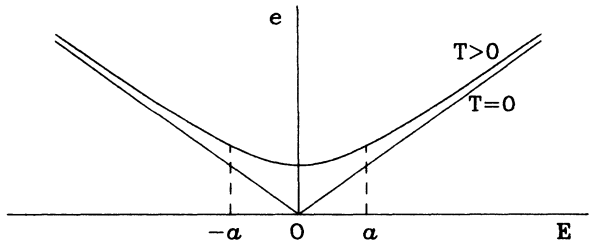

FIG. 11. Schematic plot showing the dependence of energy per rhombus on the phason strain at $T=0$ and $T>0$. Here $a=\exp(-2\varepsilon_{SS}/k_BT)$.

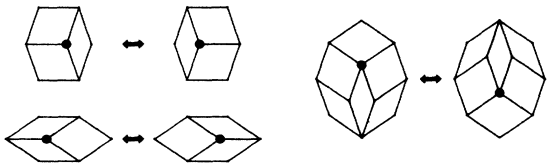

FIG. 12. Basic moves for the tiling simulations: (a) hexagon flips, and (b) an octagon flip. Solid circles indicate vertices which identify the corresponding cluster of tiles.

hexagon according to a probability

$$w=\begin{cases}\exp(-\beta\Delta E), & \text{if } \Delta E>0\ ,\\ 1, & \text{otherwise}\ .\end{cases} \tag{6.1}$$

Here ΔE is the energy cost for performing the flip. The case with octagon flips is done following a similar procedure.

Let χ_i and χ_j be two tilings related by a single flip, and

$$\Delta E=E(\chi_j)-E(\chi_i)\geq 0\ .$$

Suppose the total number of vertices in the system is N, then the transition probability

$$P(\chi_i\rightarrow\chi_j)=\exp(-\beta\Delta E)/N\ ,$$

whereas $P(\chi_j\rightarrow\chi_i)=1/N$. Thus, the detailed balance relation

$$P(\chi_i\rightarrow\chi_j)=P(\chi_j\rightarrow\chi_i)\exp(-\beta\Delta E)\ , \tag{6.2}$$

is fulfilled.

For tilings whose energy depends on the arrow configuration, single rhombus flips should be included in addition to the hexagon flips. This step is not necessary in simulating the infinite-temperature random tilings, as well as the four-vertex tiling.

In order for the above algorithm to generate the equilibrium distribution of a given ensemble, there must be a nonzero transition probability to any tiling configuration in the ensemble from a given one. Using the "dual-grid" representation of rhombus tilings,[24,38] it is possible to show that the hexagon flips, which correspond to shifting the dual lines locally, is sufficient for reaching any other configuration starting from a given one, under proper boundary conditions.

B. System characteristics

In this subsection we discuss various aspects of the tiling systems studied in our simulations. Since our main interest is the property of pentagonal quasicrystal phase, most of the systems we studied are specifically chosen to contain the smallest average phason strain at a given system size, though due to the periodic boundary conditions, it is impossible to eliminate the strain $\mathbf{E}$ completely. In addition to systems with minimal phason strain, we also looked at a few other systems at larger strain in order to understand the effect of strain on our results.

A periodic tiling can be constructed from a periodic, uniform dual grid. We choose the dual grid to be the intersection of (four-dimensional) lattice planes of the 5D hypercubic lattice at constant n_α with a 2D hypersurface spanned by two vectors

$$\begin{aligned}\mathbf{M}^{(1)}&=\{M_\alpha^{(1)}\}=(P,0,-P,-Q,Q)\ ,\\ \mathbf{M}^{(2)}&=\{M_\alpha^{(2)}\}=(0,P,Q,-Q,-P)\ ,\end{aligned} \tag{6.3}$$

where P and Q are integers. Note that this hypersurface is normal to the h_z direction $\hat{\mathbf{a}}^{(5)}$ [see Eq. (2.7)], thus there is no average $\mathbf{E}_z$ strain in the system. Once the grid lines are given, standard methods can be used to construct the tiling (see Ref. 24).

The basis vectors of the periodic tiling are given by

$$\begin{aligned}\mathbf{R}^{(1)}&=\sum_{\alpha=0}^{4}M_\alpha^{(1)}\hat{\mathbf{e}}_\alpha^{\parallel}\\ &=(P\tau+Q)\left[\frac{2\tau-1}{2},-\tau^{-1}\sin\frac{\pi}{5}\right]\ ,\\ \mathbf{R}^{(2)}&=\sum_{\alpha=0}^{4}M_\alpha^{(2)}\hat{\mathbf{e}}_\alpha^{\parallel}=(P\tau+Q)\left[0,2\sin\frac{\pi}{5}\right]\ ,\end{aligned} \tag{6.4}$$

Since $|\mathbf{R}^{(1)}|=|\mathbf{R}^{(2)}|$, the unit cell has a rhombic shape. This rhombic cell is used as a finite system in our simulations. Periodic boundary conditions are used.

The shift in $\mathbf{h}$ across the system along $\mathbf{R}^{(1)}$ and $\mathbf{R}^{(2)}$ is given by

$$\begin{aligned}\mathbf{H}^{(1)}&=\sum_{\alpha=0}^{4}M_\alpha^{(1)}\hat{\mathbf{e}}_\alpha^{\perp}=(P-Q\tau)\left[\frac{2\tau-1}{2},\tau\sin\pi/5\right]\ ,\\ \mathbf{H}^{(2)}&=\sum_{\alpha=0}^{4}M_\alpha^{(2)}\hat{\mathbf{e}}_\alpha^{\perp}=(P-Q\tau)(0,2\sin\pi/5)\ ,\end{aligned} \tag{6.5}$$

respectively. Using Eq. (2.11) we obtain the average phason strain

$$\mathbf{E}=\frac{Q^2+PQ-P^2}{(P\tau+Q)^2}\begin{bmatrix}1 & 0\\ 2\sin 2\pi/5 & \tau\end{bmatrix}\ . \tag{6.6}$$

A sequence of approximate pentagonal tilings can be obtained by taking

$$P=F_k,\quad Q=F_{k-1}\ , \tag{6.7}$$

where F_k are Fibonacci numbers satisfying the recursion relation

$$F_k=F_{k-1}+F_{k-2} \tag{6.8}$$

with $F_0=0$, $F_1=1$. The number of tiles in such a system is given by

$$N_k=F_{2k+1}+2F_{2k}\ . \tag{6.9}$$

Systems of 76, 199, 521, 1364, and 3571 tiles are obtained for k ranging from 4 to 8. They are used in most of our studies reported below.

Using (6.7), the prefactor of the strain matrix in (6.6) takes the form,

$$\frac{F_{k-1}^2+F_kF_{k-1}-F_k^2}{(F_{k-1}+F_k\tau)^2}=(-1)^k\tau^{-2k}$$
$$=(-1)^k\tau N_k^{-1}+O(N_k^{-3})\ . \quad (6.10)$$

Thus, the phason strain **E** is inversely proportional to the number of tiles in the system under the special choice (6.7).

C. Simulations of binary and unconstrained random tilings

The purpose of these two simulations is to establish the existence of quasi-long-range translational order in random tilings of the plane by Penrose rhombuses, thus confirming an earlier conjecture by Elser and Henley. The starting configurations of our simulations are chosen to be the periodic tilings mentioned above, with h_z being integers from 1 to 4. In the case of binary random tilings, where the h_z coordinate is restricted to three consecutive integers, the procedure is followed by a sequence of hexagon flips to eliminate vertices with, say, $h_z=4$. After an initial equilibration stage, which typically consists of 2000 Monte Carlo (MC) sweeps, data is gathered every 10–50 MC sweeps over a total run of 20 000–50 000 MC sweeps. (An MC sweep consists of one basic Monte Carlo move per vertex.) Correlation between successive data points is taken into account in estimating the error bars on the statistical averages (2.30)–(2.32).

As a test of the algorithm, we applied the hexagon flip scheme to the 60° rhombus-tiling model, where an exact expression for the elastic constant is known.[39] The logarithmic behavior of phason fluctuations was indeed observed. The agreement between the numerically determined elastic constant and the exact value is better than the estimated error bars, which is about 2%.

Figure 13 shows the **h** fluctuation data for the binary (solid circles) and unconstrained (open circles) random tilings, and h_z fluctuation data (triangles) for the unconstrained random tiling, computed using Eqs. (2.30) and (2.31). [To eliminate effects due to a small phason strain, the perpendicular space coordinate **h** is calculated using (2.21).] Error bars on the data are roughly represented by the size of plotting symbols. The logarithmic behavior over the range of sizes studied is apparent. The slopes for the three lines are determined to be 0.254±0.010, 0.265±0.010, and 0.276±0.015, respectively. The corresponding elastic constants, defined through (2.30) and (2.31), are listed in Table I.

TABLE I. Phason elastic constants and entropy per tile s_∞ for three different random tilings.

Tiling	K	K_z	s_∞/k_B
Unconstrained random	0.600±0.025	0.288±0.016	≃0.5[a]
Binary random	0.626±0.025[b]	∞	0.1928±0.0004[c]
Four-vertex, $T=\infty$	0.740±0.032	∞	0.393±0.002

[a]Estimated by Henley (Ref. 12).
[b]Widom *et al.* obtained a value 0.600±0.006 from a transfer-matrix study (Ref. 15).
[c]Widom *et al.* (Ref. 15).

We also measured scattering intensities at a number of peaks. The data for the unconstrained random tilings are shown in Fig. 14, where points corresponding to the same peak (with phason strain taken into account) are connected with straight lines. Points with $Q_{Pz}=0$ are represented by solid circles, and those with $Q_{Pz}=\pm 2\pi/5$ are represented by open circles. The nearly linear behavior of data in each group on the log-log plot confirms the finite-size scaling relation (2.33), thus providing direct evidence for the quasi-long-range translational order in the tiling system. The slopes of the lines are determined

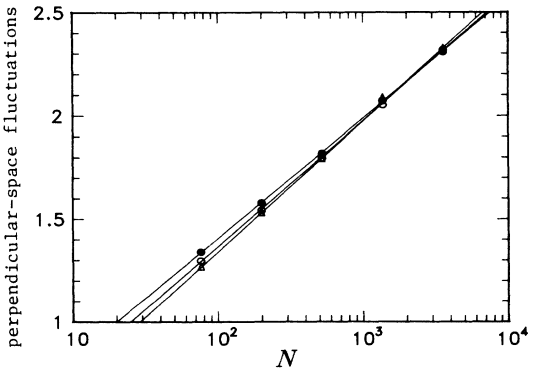

FIG. 13. Mean-square deviation of the perpendicular-space coordinates [see Eqs. (2.30) and (2.31)] vs logarithm of system size N for **h** of the binary tiling (solid circles), **h** of the unconstrained tiling (open circles), and h_z of the unconstrained tiling (open triangles).

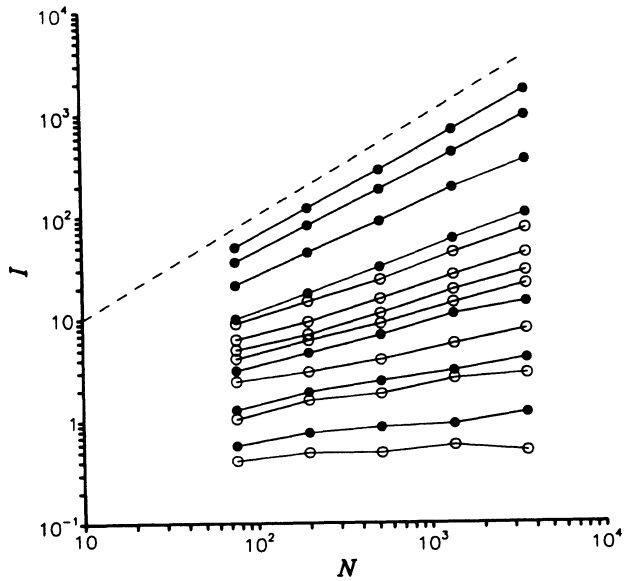

FIG. 14. Diffraction intensities vs logarithm of system size N for the unconstrained random tiling at a number of peaks studied. Points of the same peak are connected. Solid circles correspond to $Q_z=0$, and open circles, $Q_z=\pm 2\pi/5$. A line (dashed) with slope 1 is drawn for comparison.

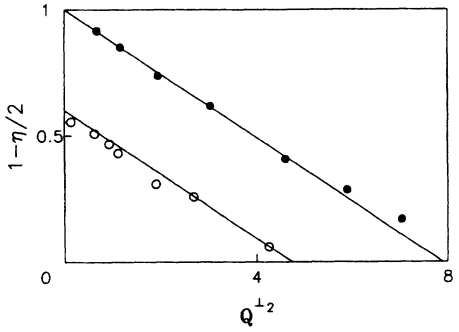

FIG. 15. Slopes for each set of data shown in Fig. 14 vs the square of the phason momentum $\mathbf{Q}^{\perp}$, with $Q_z=0$ (solid circle) and $\pm 2\pi/5$ (open circle). The lines are drawn using Eq. (2.34) with K and K_z taken from Table I.

and plotted against $|\mathbf{Q}^{\perp}|^2$, as shown in Fig. 15. Data with $Q_{Pz}=0$ and $\pm 2\pi/5$ fall on two separate straight lines, which are drawn using Eq. (2.34) and the value for K and K_z taken from Table I.

The fact that the elastic constant K for the two random tilings is almost identical is an interesting and intriguing result. One can plausibly relate this behavior to the universality of elastic constant in uniaxial striped domain-wall systems.[40] The latter case can be represented by a quantum mechanical system of one-dimensional fermions. Using a free-fermion approximation, a universal elastic constant can be obtained. Adding short-range interactions among the fermions may or may not change the elastic constant. Given the various topological properties of the rows, one may plausibly formulate the equilibrium statistical theory of rhombus tilings in the one-dimensional fermion system language. Further work is needed to quantify this connection.

D. Simulation of four-vertex tilings

The arguments given in Secs. IV and V suggest that the logarithmic dependence of **h** fluctuations on the system size, observed for the random-tiling models, should continue down to $T=0$ in the Penrose model. In this section we present simulation data on the four-vertex tiling model which support the heuristic arguments and results from the RG analysis.

We recall that the four-vertex model is defined by the energy (2.2) with $\varepsilon_{SS}=1$ and $\varepsilon_{SD}=\varepsilon_{DD}=+\infty$, thus only unmatched single arrows are allowed at any T, including $T=\infty$ (by convention).

The simulation was carried out as described in the previous subsection. Data were taken following a heating sequence, from $\beta=4$ to 2.5 at increment $\Delta\beta=0.5$, and from 2.5 to 0 at $\Delta\beta=0.25$. As before, at each temperature the system was equilibrated for a period of 2000 MC sweeps before data were taken. This seems to be adequate, as no transient behavior was observed. We did some cooling runs to check the presence of hysteresis effects, too. Within the statistical errors, the data so obtained agree well with those from heating studies. The lowest energy state [containing two or more $(SS)^-$ bonds due to the periodic boundary conditions, which can be calculated using Eqs. (3.3) and (6.6)] is always obtained as we continue the simulation down to very low temperatures.

Carrying out the simulation at $\beta>4$ (or $T<0.25$) is hindered by both the small probability $e^{-2\beta}$ for creating a pair of $(SS)^-$ bonds, and the large system size (approximately $e^{2\beta}$ tiles) needed to begin to see the full effect of equilibrium phason fluctuations (see discussion in Secs. IV and V). More efficient algorithm and considerably larger system size and longer runs are needed to explore the equilibrium behavior of the model in this temperature regime.

Figure 16(a) shows part of a configuration χ obtained during a simulation of the 3571 tile system at $\beta=2$, and Fig. 16(b) a tiling obtained from χ after three inflation

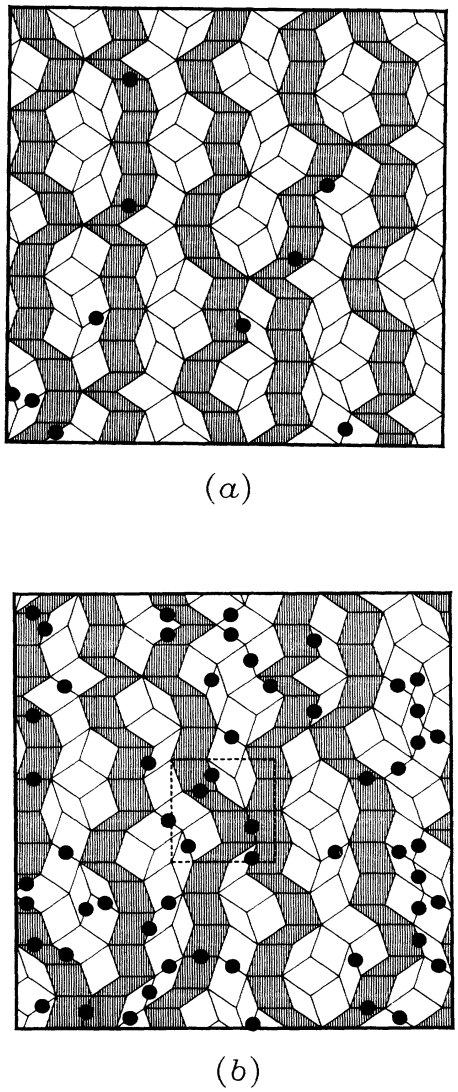

FIG. 16. A typical equilibrium configuration at $\beta=2$ from Monte Carlo simulation. (a) Part of a 3571-tile system. Traces of the quasiperiodic spacing of rows (shaded) can still be seen. (b) The whole system after three times inflation. The area enclosed by the box of dashed lines corresponds to the part shown in (a). Phason fluctuations are much more pronounced. $(SS)^-$ bonds are indicated by solid circles in both cases.

transformations (see Sec. V), plotted using the same rhombus edge length. The part of Fig. 16(b) which corresponds to the inflation of Fig. 16(a) is indicated by the box of dashed lines. All $(SS)^-$ bonds, indicated by solid circles, are located within the worms in Fig. 16(a), but not necessarily so in Fig. 16(b). Obviously, the inflation transformation carries the system to higher temperatures with a larger density of $(SS)^-$ bonds.

We have shaded rhombus rows which have an average vertical orientation. In a Penrose tiling, these rows divide the system into a quasiperiodic sequence of wide and narrow strips. This behavior can still be identified in Fig. 16(a), but is absent in Fig. 16(b). This implies that, even at very low temperatures, the quasiperiodicity associated with the ground state is lost on sufficiently large length scales. From the transverse displacement of rows one can get a rough estimate on the phason fluctuations, which are much more pronounced in the inflated tiling.

In the following we present a more quantitative comparison between Monte Carlo simulation results and predictions of the RG analysis. The quantity which can be most accurately determined in our simulations is the energy per tile $e(N)$ for a system of size N, which also gives the density of $(SS)^-$ bonds. Figure 17 shows $e(N)$ at $\beta=1$ plotted against $1/N$ for the five sizes 76–3571 with minimal phason strain, and three other sizes $2^2\times 76$, $3^2\times 76$, and $2^2\times 199$. Data at a given phason strain **E** are connected by a straight line. The lines are nearly parallel to each other, indicating a finite-size correction which is approximately linear in $1/N$, with a slope independent of **E** (for small **E**). This behavior is generally expected for 2D systems described by a square-gradient free energy. The upward increasing behavior of $e(N)$ with N can be plausibly interpreted as due to the long-wavelength cutoff of phason fluctuations, thus reducing the number of $(SS)^-$ bonds in smaller systems. The extrapolated value for the infinite tilings is larger for systems with large phason strain, showing that the quasicrystal phase has the lowest (free) energy.

Figure 18 shows the energy per tile extrapolated for the infinite system at zero phason strain. The error bar

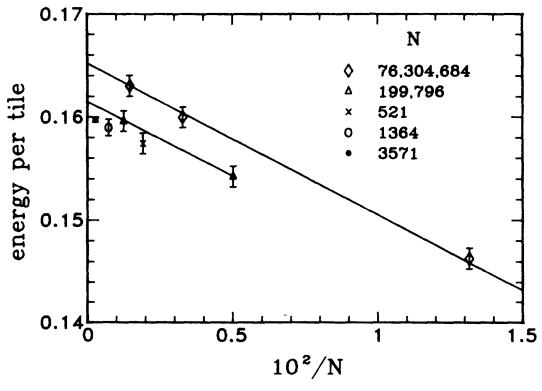

FIG. 17. Energy per tile vs inverse system size at $\beta=1$ for tilings at various phason strain. Data at the same strain are connected by a straight line.

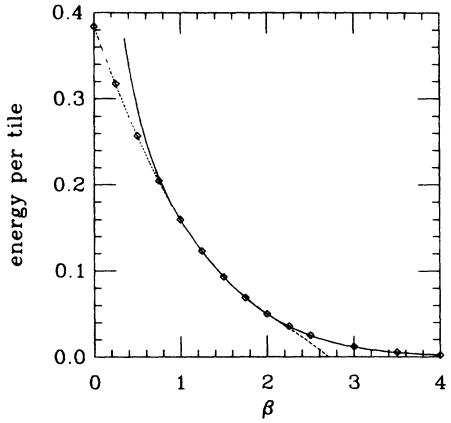

FIG. 18. Energy per tile vs inverse temperature β. The solid and the dashed lines are drawn using the fits Eqs. (6.11) and (6.12), respectively.

on all data points is about 0.5×10^{-3}. The data fit well with

$$e(\beta)=(2\beta-1.3838)e^{-2\beta}+(2\beta+2.1820)e^{-4\beta}\,, \tag{6.11}$$

in the range $1<\beta<4$, as shown by the solid line. This is to be compared with the derivative of (5.17) with respect to β. For $\beta<1$ the data fall on the curve

$$e(\beta)=0.3841-0.279\beta+0.0436\beta^2 +0.0164\beta^3-0.0051\beta^4\,, \tag{6.12}$$

shown by the dashed line.

Figure 19 shows the heat capacity

$$c/k_B=k_B^{-1}\frac{de}{dT}=\beta^2(\langle e^2\rangle-\langle e\rangle^2)\,. \tag{6.13}$$

The two curves on the figure are obtained by taking derivatives of (6.11) (solid line) and (6.12) (dashed line), which fit well with the data within each temperature range.

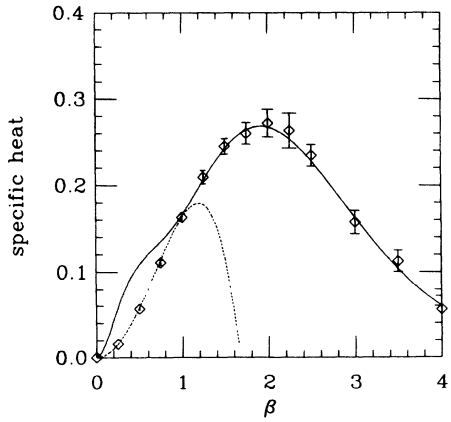

FIG. 19. Specific heat vs inverse temperature β. The solid and dashed lines are drawn using the derivatives of Eqs. (6.11) and (6.12), respectively.

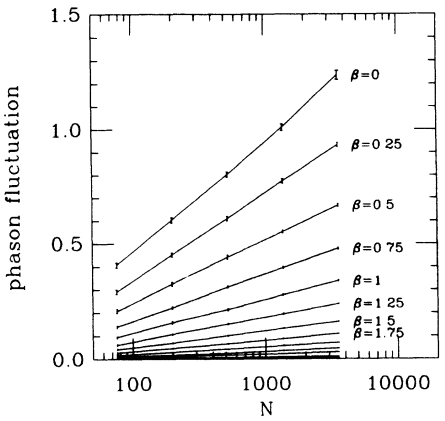

FIG. 20. Mean-square deviation of the perpendicular-space coordinates [see Eq. (2.30)] vs logarithm of system size N for the four-vertex tiling model at various temperatures. Data at the same temperature are connected with straight lines.

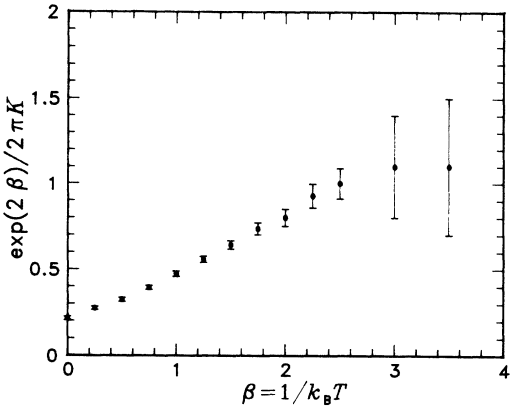

FIG. 22. Slopes for each set of data shown in Figs. 20 and 21, multiplied by $e^{2\beta}$, and plotted vs β.

The free energy and entropy can be obtained by integrating (6.11) and (6.12). For instance, the entropy per tile of the four-vertex tiling at infinite temperature is given by

$$s_\infty/k_B=\int_0^\infty e(\beta)d\beta=0.393\pm0.002\ , \tag{6.14}$$

which is about twice the value for the binary tiling determined by Widom *et al.* using a transfer matrix method (see Table I).[15]

Figures 20 and 21 show the average fluctuation of **h** plotted against N on a similog scale, at high and low temperatures, respectively. [We have subtracted out the corresponding zero-temperature value.] Points at the same temperature are connected by straight lines. The logarithmic behavior is observed for $\beta\leq 2.5$, and reasonably accurate phason elastic constant can be determined. At lower temperatures, one still sees the definite trend of increasing phason fluctuations with system size, though the data is not accurate enough to provide a meaningful test of (2.30).

The slope of lines in Figs. 20 and 21, multiplied by $e^{2\beta}$, is plotted in Fig. 22. The data show a slightly upward trend as β increases, instead of the predicted behavior (5.18).

We also studied the dependence of scattering intensities on system size, which exhibits the expected power-law behavior. Figure 23 shows an example at $\beta=0.5$, where the exponent η is plotted against $|\mathbf{Q}^\perp|^2$. Note that since there is no roughening in h_z direction, all data points fall on a single line, in contrast to the behavior shown in Fig. 15.

From the above analysis of phason fluctuations, scattering intensities, and the behavior of equilibrium configurations under inflation transformations, we conclude that the phason fluctuations lead to the roughening of the deBruijn surface in the **h** direction for β up to at least 3. The logarithmic dependence on system size at these temperatures supports the scenario that long-wavelength **h** fluctuations are described by a square-gradient free energy. The behavior of the energy per tile

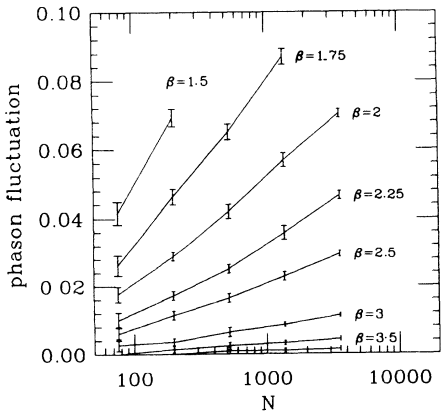

FIG. 21. An enlargement of the low temperature region in Fig. 20.

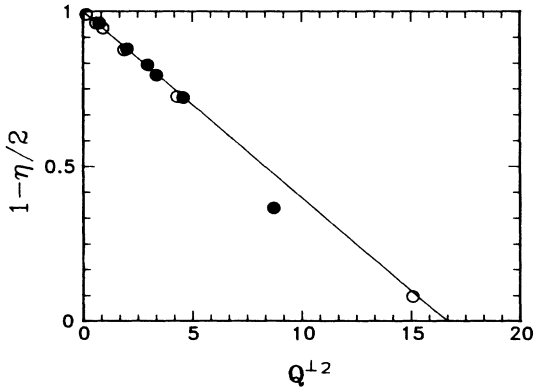

FIG. 23. Finite-size scaling exponent of the scattering intensity vs the square of the phason momentum $\mathbf{Q}^\perp$ for the four-vertex tiling at $\beta=0.5$ [see Eq. (2.33) and Fig. 15]. A line is drawn using Eq. (2.34) with K given in Fig. 22. Solid circle: $Q_z=0$. Open circle: $Q_z=\pm 2\pi/5$.

and phason elastic constant at low temperatures agree well with predictions of the RG analysis. Finally, we mention that a recent Monte Carlo study by Strandburg and Dressel on a similar Penrose rhombus tiling model[41] indicated a roughening transition in $\mathbf{h}$ at $\beta \simeq 2.5$, in disagreement with our result.

VII. CONCLUSIONS

Our paper presents one of the first detailed studies of the equilibrium properties of a 2D matching-rule-based quasicrystal model. The model exhibits quite interesting configurational disordering behavior, connected to the quasiperiodicity of the ground state. We have carried out detailed analysis of phason fluctuations and long-range translational order in the system, and the behavior of phason elastic (free) energy and other thermodynamic functions. A close relationship between the tiling model and the general surface roughening phenomena is established.

We elaborated on the unusual zero-temperature phason elasticity suggested by Socolar *et al.* for unit-cell quasiperiodic crystals. Both analytic calculations and heuristic arguments are presented, which give a linear dependence of the phason elastic energy on the strain. The heuristic argument offers an intuitive understanding of how the linear form arises in a unit-cell model which possesses a continuous phason translation symmetry. We also pointed out a feature of the Penrose model, whose energy does not contain a lock-in term which favors periodic tilings.

Through real-space RG analysis and Monte Carlo simulations we were able to show that the unusual $T=0$ phason elastic energy changes to the usual quadratic form at any $T>0$ and sufficiently small strain $|\mathbf{E}| \leq e^{-2\beta\epsilon_{SS}}$, where $e^{-\beta\epsilon_{SS}}$ is the Boltzmann weight for a single matching-rule violation (defect). Intuitively, this is understood in terms of the large entropy available, in a quasicrystal configuration, for each of the defects which contributed to the $T=0$ phason elastic energy. This large entropy leads to the vanishing of the free energy for the defects, hence the disappearance of the linear term in the elastic energy. The crossover from the linear to the quadratic form occurs when the number of thermally excited defects exceeds the number of strain forced ones.

A global picture for the melting of the ground-state quasiperiodicity is provided by the real-space RG analysis. At very low temperatures the local configurations in an equilibrium tiling are essentially the same as in the ground state. Tile rearrangements on the length scale $e^{\beta\epsilon_{SS}}$, which can be seen by performing a certain number of inflation transformations, destroy the long-range translational order. As the temperature increases, each domain represented by an inflated tile breaks into smaller domains. This process continues up to infinite temperature, where a random tiling on the single rhombus scale is obtained.

Phason fluctuations in the tiling model are measured in the Monte Carlo simulations. They show a logarithmic divergence on increasing system size for the random-tiling models, and for the Penrose model at the range of temperatures studied. This is in agreement with a square-gradient description of phason fluctuations. The Fourier intensities of the equilibrium tilings also show the expected power-law dependence on system size. Though the simulation algorithm is not efficient for studying very long-wavelength phasons, which are important at very low temperatures, there is no indication that phason fluctuations will settle to a constant value with increasing system size at a low, but nonzero, temperature. We thus conclude that the random tilings and the Penrose model at any finite temperature possess quasi-long-range translational order.

The heuristic domain-wall picture for the behavior of phason strain energy presented in Sec. IV can be readily generalized to other 2D quasicrystal models, and to three dimensions. It is plausible that the 3D rhombohedron tiling with a matching-rule-based energy[7] will exhibit the same unusual $T=0$ phason elasticity as in the 2D case. However, the physics at finite temperatures can be different in the two cases. For the 2D Penrose tiling model, a defect can be placed anywhere inside a worm without increasing system energy. This was the origin for the vanishing of the linear strain term in the elastic energy at finite temperatures and sufficiently small strain. In three dimensions, we may imagine the worms being replaced by sheets of rhombohedra, and the point defects which arise from a phase shift across the system being replaced by line defects in the sheets. If the matching-rule energy is such that a rigid translation of the line on the sheet does not cost energy (except perhaps at the ends of the line), but producing a jag on the line does, then one expects the linear form of elastic energy to remain up to a finite temperature. At sufficiently high temperatures it should be possible for the line defects to gain enough entropy to overcome their creation energy. A quadratic phason elastic free energy is then expected. It would be interesting to see whether the vanishing of the linear term in the strain energy is accompanied by a phase transition in the quasicrystal phase.

We believe the real-space RG analysis can be extended to a general class of classical systems with a quasiperiodic ground state, though a lack of inflation symmetry may introduce additional complications. The basic idea can already be seen in the analysis of low-temperature behavior of one-dimensional incommensurate systems by Vallet *et al.*, where they considered a real-space RG scheme based on the quasiperiods (continued fraction expansion) of the incommensurate ground state.[42]

Finally, we comment on possible implications of our results to the physical properties of real quasicrystals. It is clear that studies of the equilibrium behavior of phasons is an indispensible step toward a complete theory of quasicrystal formation and stability. The picture of a continuous disordering of an ideal quasiperiodic structure into random tilings, on an ever decreasing length scale as temperature increases, may provide a useful framework for understanding and analyzing various structural properties of equilibrium quasicrystals. The two forms of phason elastic energy can be useful for constructing sample phase diagrams of quasicrystal and other nearby phases, using chemical potential as a controlling parame-

ter, so that the thermodynamic relationship among the quasicrystal phase and other incommensurately modulated, and large unit-cell periodic phases can be obtained. Lastly, we point out that thermal phason fluctuations can have a profound effect on electronic, magnetic, and surface properties of quasicrystals. In the latter case, the work of Lipowsky and Henley suggested that surface roughness is qualitatively different for a quasiperiodic-crystal quasicrystal and a random-tiling quasicrystal.[43]

Note added in proof. After submission of the paper we became aware of an article by Kalugin where a heuristic argument for the roughening of the deBruijn surface similar in spirit to ours was presented.[44] A discussion of matching rules has been recently formulated by Socolar for a general class of tiling models.[45] In particular, the question of matching rules for the 3D Penrose tiling was addressed. Some of his considerations are parallel to those presented in Sec. III of this work.

ACKNOWLEDGMENTS

We would like to acknowledge useful discussions with V. Elser, K. J. Strandburg, M. Kardar, and D. E. Wolf, and computer assistance from S. Johnson. This study was initiated when both of us were visitors at Institute for Theoretical Physics, University of California, Santa Barbara. One of us (L.T.) wishes to thank the Materials Science Division, Argonne National Laboratory for their hospitality, where part of the work was carried out, and Insitut für Festkörperforschung der Kernforschungsanlage Jülich, where the work was completed. This research was supported in part by the Center for Theoretical Physics and through the Board of Regents Advanced Materials Program at Texas A&M University.

APPENDIX

We present here a direct calculation of the energy per tile for a four-vertex tiling under a uniform phason strain $\mathbf{E}$, constructed using the projection method. As discussed in Sec. II B, the deBruijn surface representing the tiling is globally parallel to the two vectors $\mathbf{b}^{(1)}$ and $\mathbf{b}^{(2)}$ given in Eq. (2.13). As in the case of unstrained tilings, one can define a "tilted" perpendicular space globally orthogonal to the deBruijn surface, which is a 3D plane spanned by

$$\begin{aligned}\tilde{\mathbf{a}}^{(3)}&=\hat{\mathbf{a}}^{(3)}-E_{11}\hat{\mathbf{a}}^{(1)}-E_{12}\hat{\mathbf{a}}^{(2)}\ ,\\ \tilde{\mathbf{a}}^{(4)}&=\hat{\mathbf{a}}^{(4)}-E_{21}\hat{\mathbf{a}}^{(1)}-E_{22}\hat{\mathbf{a}}^{(2)}\ ,\end{aligned}\tag{A1}$$

and $\hat{\mathbf{a}}^{(5)}$, where $\hat{\mathbf{a}}^{(\alpha)}$ are given by Eqs. (2.5)–(2.7). Let $W(\{\xi_\alpha\})$ be the projection of a 5D unit cube

$$\xi_\alpha \le x_\alpha < \xi_\alpha+1,\quad \alpha=0,\ldots,4\ ,\tag{A2}$$

into the tilted perpendicular space. The "window" $W(\{\xi_\alpha\})$ specifies a 2D projection strip in the 5D space, which consists of points whose projection into the tilted perpendicular space lie in $W(\{\xi_\alpha\})$. We assert without proof that, as in the case of Penrose tilings, projection of 5D hypercubic lattice sites (with lattice spacing equal to unity) which lie within the strip into the physical space, gives a complete set of vertices of a generalized Penrose rhombus tiling.[27] (Special attention should be paid to lattice sites which sit on the boundary of the strip.)

The shape of the 3D window $W(\{\xi_\alpha\})$ has been given by Jarić for the case $\mathbf{E}=0$.[27] At nonzero strain the rhombic icosahedron is distorted from its regular fivefold symmetric shape. Since the h_z coordinate of the 5D lattice sites takes only integral values, for $\mathbf{E}_z=0$ the projection of lattice sites within the strip is distributed on five 2D sections of the rhombic icosahedron, corresponding to five successive values of h_z. If one takes $\sum\xi_\alpha=0$ (or any other integral value), the number of nonempty 2D sections reduces to four. Consequently a four-vertex tiling is obtained. In the following we shall restrict ourselves to this case and assume h_z to be from 1 to 4.

The projection window can be alternatively specified in terms of the $\tilde{\mathbf{h}}$ coordinates introduced in Sec. II C, Eq. (2.21). The two orthogonal components of $\tilde{\mathbf{h}}$ are given by the projection of a 5D vector $\{x_\alpha\}$ onto $\tilde{\mathbf{a}}^{(3)}$ and $\tilde{\mathbf{a}}^{(4)}$, respectively, i.e.,

$$\tilde{\mathbf{h}}(\{x_\alpha\})=\sum_\alpha x_\alpha\tilde{\mathbf{e}}_\alpha^{\perp}\ ,\tag{A3}$$

where

$$\tilde{\mathbf{e}}_\alpha^{\perp}=\hat{\mathbf{e}}_\alpha^{\perp}-\mathbf{E}\hat{\mathbf{e}}_\alpha^{\parallel}\ .\tag{A4}$$

The window is then specified by four domains D_1, D_2, D_3, and D_4 on the $\tilde{\mathbf{h}}$ plane, where D_k is the set of points $\tilde{\mathbf{h}}$ obtained from (A3) for $\{x_\alpha\}$ belong to the 5D unit cube (A2) and subjected to the constraint

$$h_z(\{x_\alpha\})=\sum_\alpha x_\alpha=k\ .\tag{A5}$$

In general, we define a *shifted* domain $D_k(\tilde{\mathbf{h}}_0)$ to be the set of points $\tilde{\mathbf{h}}$ such that $\tilde{\mathbf{h}}-\tilde{\mathbf{h}}_0\in D_k$.

The neighboring bond configuration of a vertex $\mathbf{r}=\sum_\alpha n_\alpha\hat{\mathbf{e}}_\alpha^{\parallel}$ in the tiling constructed above can be obtained as follows. Suppose $h_z(\mathbf{r})=k$, then $\tilde{\mathbf{h}}(\mathbf{r})$ lies in D_k. The point $\mathbf{r}+\hat{\mathbf{e}}_\alpha^{\parallel}$ is also a vertex of the tiling if and only if $\tilde{\mathbf{h}}(\mathbf{r})+\tilde{\mathbf{e}}_\alpha^{\perp}$ lies in D_{k+1}, or $\tilde{\mathbf{h}}(\mathbf{r})$ lies in the domain $D_{k+1}(-\tilde{\mathbf{e}}_\alpha^{\perp})$. Hence, the presence of a bond in the direction $\hat{\mathbf{e}}_\alpha^{\parallel}$ at $\mathbf{r}$ is determined by whether $\tilde{\mathbf{h}}(\mathbf{r})$ lies in the overlapping region of D_k and $D_{k+1}(-\tilde{\mathbf{e}}_\alpha^{\perp})$. Similarly, the presence of a bond in the direction $-\hat{\mathbf{e}}_\alpha^{\parallel}$ at $\mathbf{r}$ is determined by whether $\tilde{\mathbf{h}}(\mathbf{r})$ lies in the overlapping region of D_k and $D_{k-1}(\tilde{\mathbf{e}}_\alpha^{\perp})$. By plotting D_k and ten other domains $D_{k+1}(-\tilde{\mathbf{e}}_\alpha^{\perp})$ and $D_{k-1}(\tilde{\mathbf{e}}_\alpha^{\perp})$, $\alpha=0,\ldots,4$ (five for $k=1$ or 4), the neighboring bond configuration for each point on D_k is obtained.

Figure 24 shows the construction applied to (a) D_1, and (b) D_2 for a Penrose tiling. The two domains D_1 and D_2 correspond to regions enclosed by the heavy lines in Fig. 24(a) and Fig. 24(b), respectively, while other domains are shown by the dashed lines. Eight non-symmetry-related domains within D_1 and D_2 are obtained, corresponding to eight different local bond configurations, as discussed previously by deBruijn,[24] and by Jarić.[27] The other two domains D_3 and D_4 are related to D_2 and D_1 by inversion.

We now consider a strained four-vertex tiling. Since

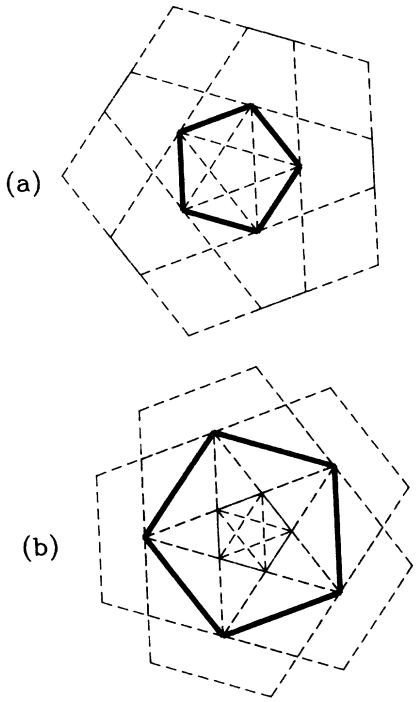

FIG. 24. Overlapping pattern of (a) D_1 and (b) D_2 (region enclosed by the heavy lines) with other window domains for the Penrose tiling. D_1 is divided into three kinds of non-symmetry-related subdomains, while there are five different kinds on D_2. Points within each subdomain have the same neighboring bond configuration in the tiling.

D_0 and D_5 are empty sets, only bonds which are possible are $\hat{\mathbf{e}}_\alpha^{\parallel}$ for points on D_1, and $-\hat{\mathbf{e}}_\alpha^{\parallel}$ for points on D_4. Thus, the neighboring bond configuration of a point on D_1 and D_4 belongs necessarily to one of three types, queen, king, and star, corresponding to three, four, and five outgoing bonds. Indeed, all subdomains on D_1 and D_4 can be made to correspond to the subdomains in Fig. 24(a).

The situation concerning D_2 and D_3 is different. Figure 25 is an example of D_2, which is divided into a set of subdomains by the boundaries of ten other domains. The shaded region cannot be identified with any of the subdomains in Fig. 24(b), thus representing points with local bond configurations not found in a Penrose tiling. Each such local configuration contains one or more $(SS)^-$ bonds.

The shaded area in Fig. 25 can be decomposed into five parallelograms, each representing an $(SS)^-$ bond in a given direction. Figure 26 is an enlargement of the overlapping region of D_2 with $D_3(-\mathbf{e}_0^{\perp})$, which gives rise to an SS bond in $\hat{\mathbf{e}}_0^{\parallel}$ direction. The area shaded by 45° lines in the figure is the overlap of this domain with $D_3(-\mathbf{e}_1^{\perp})$ or $D_1(\mathbf{e}_3^{\perp})$, so that we have a bond along either the $\hat{\mathbf{e}}_1^{\parallel}$ or $-\hat{\mathbf{e}}_3^{\parallel}$ direction at the same time. The overlap of the domain with $D_3(-\mathbf{e}_4^{\perp})$ or $D_1(\mathbf{e}_2^{\perp})$, is shaded by $-45°$ lines, indicating the presence of a bond along either the $\hat{\mathbf{e}}_4^{\parallel}$ or $-\hat{\mathbf{e}}_2^{\parallel}$ direction. In the region where the two shaded areas overlap, a situation corresponding to one of the three cases C_1, C_2, or C_3 shown in Fig. 3(a) is obtained.

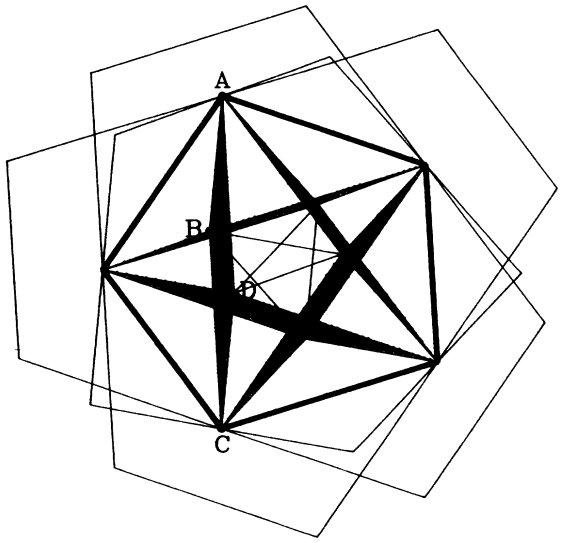

FIG. 25. Overlapping pattern of D_2 (region enclosed by the heavy lines) with other window domains for a strained tiling. The shaded area does not correspond to any of the subdomains on Fig. 24(b), thus representing vertices where the neighboring bond configuration is not found in a Penrose tiling.

Thus, one has a pair of matched single arrows. This is also true for the white region which is covered by neither of the two shaded areas. The remaining region inside the domain, which is covered by only one of the two shaded areas, gives rise to an $(SS)^-$ bond of the type C_4, C_5, or C_6 shown in Fig. 3(b). The four vertices of the parallelogram are given by $A=\mathbf{e}_1^{\perp}+\mathbf{e}_3^{\perp}$, $B=\mathbf{e}_3^{\perp}+\mathbf{e}_4^{\perp}$, $C=\mathbf{e}_2^{\perp}+\mathbf{e}_4^{\perp}$, and $D=\mathbf{e}_1^{\perp}+\mathbf{e}_2^{\perp}$. From them we obtain the area of the parallelogram

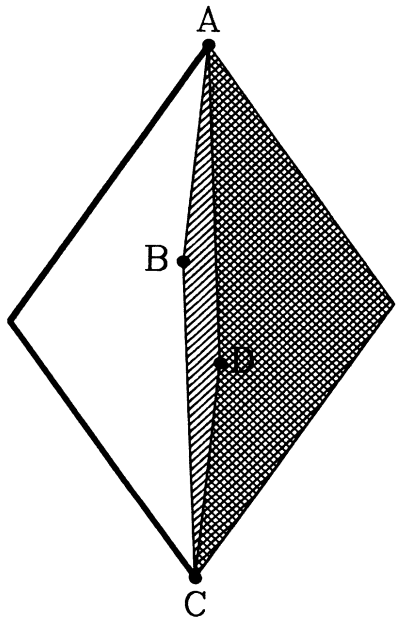

FIG. 26. Enlargement of the left corner on Fig. 25. The area shaded by 45° lines is covered by either $D_3(-\mathbf{e}_1^{\perp})$ or $D_1(\mathbf{e}_3^{\perp})$, while the area shaded by $-45°$ lines is covered by either $D_3(-\mathbf{e}_4^{\perp})$ or $D_1(\mathbf{e}_2^{\perp})$.

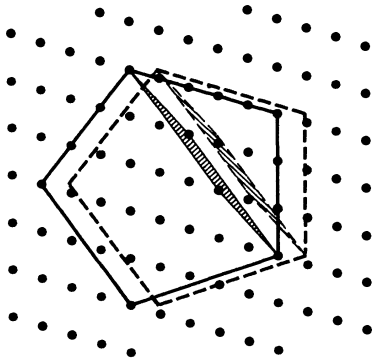

FIG. 27. Projection of 5D lattice sites to a commensurate perpendicular space, along with the window D_2. The area enclosed by thick dashed lines is the window of a shifted projection strip. Note that since the shaded region is a unit cell of the projected periodic structure, it always contains one solid circle, independent of the window position.

$$\begin{aligned}\sigma_{\alpha=0}&=|(\tilde{\mathbf{e}}_2^{\perp}-\tilde{\mathbf{e}}_3^{\perp})\times(\tilde{\mathbf{e}}_4^{\perp}-\tilde{\mathbf{e}}_1^{\perp})|\\&=|[\mathbf{e}_2^{\perp}-\mathbf{e}_3^{\perp}-\mathbf{E}(\mathbf{e}_2^{\parallel}-\mathbf{e}_3^{\parallel})]\times[\mathbf{e}_4^{\perp}-\mathbf{e}_1^{\perp}-\mathbf{E}(\mathbf{e}_4^{\parallel}-\mathbf{e}_1^{\parallel})]|\\&=(\tau+\tau^{-1})|(\mathbf{e}_4^{\perp}-\mathbf{e}_1^{\perp})\times\mathbf{E}(\mathbf{e}_4^{\parallel}-\mathbf{e}_1^{\parallel})|\\&=5|\mathbf{e}_0^{\parallel}\times\mathbf{E}^T\mathbf{e}_0^{\perp}|\ ,\end{aligned}\tag{A6}$$

where we used (A4). Equation (A6) applies generally to bonds in other directions with 0 replaced by α in the final expression.

For a tiling whose $\tilde{\mathbf{h}}(\mathbf{r})$ distribute densely and uniformly on the four domains D_k, the number of $(SS)^-$ bonds per vertex is given by the ratio of $\sum_\alpha\sigma_\alpha$ to the total area of the four domains

$$\begin{aligned}\sigma_T&=\sum_\alpha[\tilde{\mathbf{e}}_{\alpha+2}^{\perp}\times\tilde{\mathbf{e}}_{\alpha}^{\perp}+(\tilde{\mathbf{e}}_{\alpha}^{\perp}+\tilde{\mathbf{e}}_{\alpha+2}^{\perp})\times(\tilde{\mathbf{e}}_{\alpha}^{\perp}+\tilde{\mathbf{e}}_{\alpha-2}^{\perp})]\\&=5(2+\tau)\sin\frac{2\pi}{5}(1-\tau^{-3}\det\mathbf{E})\ ,\end{aligned}\tag{A7}$$

which yields Eq. (3.3).

One might question the validity of the result (3.3) when the projection of 5D lattice sites obtained from a tiling does not distribute densely and uniformly over the four domains. In particular, a periodic tiling can correspond to a situation where the differences $\tilde{\mathbf{e}}_\alpha^{\perp}-\tilde{\mathbf{e}}_\beta^{\perp}$ become lattice vectors of a 2D periodic structure. Projection of 5D lattice sites on the $\tilde{\mathbf{h}}$ plane will then sit on the 2D lattice points, as illustrated by the dots in Fig. 27. However, since the projection of a given 5D lattice site (which may or may not lie in the strip) does not depend on $\{\xi_\alpha\}$, while changing $\{\xi_\alpha\}$ under the constraint $\sum_\alpha\xi_\alpha=0$ corresponds to shifting the window in the $\tilde{\mathbf{h}}$ plane (see Fig. 27), a dense, uniform distribution of projected points on each D_k can be obtained through properly averaging over tilings obtained from shifted windows. The total area of the four domains (A7) is proportional to the density of vertices in the tiling, which is not changed under the shift. Thus, Eq. (3.3) gives the average energy per vertex for this set of tilings. Since the same expression is also a lower bond of the energy for each individual tiling, the energy per tile must be the same for all these tilings, and is given by (3.3).

In the example shown in Fig. 27, we see that the parallelogram which corresponds to an $(SS)^-$ bond (e.g., *ABCD* in Fig. 25) is a primitive cell of the projected periodic structure. In general, as $\tilde{\mathbf{e}}_\alpha^{\perp}-\tilde{\mathbf{e}}_\beta^{\perp}$ are all lattice vectors on the $\tilde{\mathbf{h}}$ plane for a periodic tiling, each such parallelogram covers an integral number of primitive cells, so that shifting the window does not change the number of points contained in the parallelograms.

*Present address: Institut für Festkörperforschung der Kernforschungsanlage Jülich, D-5170 Jülich, West Germany.

[1]D. Shechtman, I. Blech, D. Gratias, and J. W. Cahn, Phys. Rev. Lett. **53**, 1951 (1984).

[2]D. Levine and P. J. Steinhardt, Phys. Rev. Lett. **53**, 2477 (1984).

[3]P. A. Kalugin, A. Yu. Kitaev, and L. C. Levitov, Pisma Zh. Eksp. Teor. Fiz. **41**, 119 (1985) [JETP Lett. **41**, 145 (1985)].

[4]Reports of early work on quasicrystals can be found in J. Phys. (Paris) Colloq. **47**, C3-1 (1986).

[5]For recent reviews on the subject, see *Aperiodicity and Order*, edited by M. V. Jarić (Academic, Boston, 1989), Vols. 1–3, and the reprint collection volume, *The Physics of Quasicrystals*, edited by P. J. Steinhardt and S. Ostlund (World-Scientific, Singapore, 1987). An earlier review was given by C. L. Henley, Comments Cond. Matter Phys. **13**, 59 (1987).

[6]For a historical introduction, see M. Lebrecht, Mosaic **18**, 2 (1987/88).

[7]D. Levine and P. J. Steinhardt, Phys. Rev. B **34**, 596 (1986); J. E. S. Socolar and P. J. Steinhardt, *ibid.* **34**, 617 (1986).

[8]R. Penrose, Bull. Inst. Math. Appl. **10**, 266 (1974). M. Gardner, Sci. Amer. **236**, 110 (1977).

[9]P. Kramer and R. Neri, Acta Crystallogr. A **40**, 580 (1984).

[10]A. Katz and M. Duneau, J. Phys. (Paris) **46**, C8, 31 (1985).

[11]V. Elser, Phys. Rev. Lett. **54**, 1730 (1985); in *Proceedings of the XVth International Colloquium on Group Theory in Physics*, edited by R. Gilmore and D. H. Feng (World-Scientific, Singapore, 1987), p. 162.

[12]C. L. Henley, J. Phys. A **21**, 1649 (1988).

[13]M. Widom, K. J. Strandburg, and R. H. Swendsen, Phys. Rev. Lett. **58**, 706 (1987).

[14]P. Lançon, L. J. Billard, and P. Chaudhari, Europhys. Lett. **2**, 625 (1986); P. Lançon and L. J. Billard, J. Phys. (Paris) **49**, 249 (1988).

[15]M. Widom, D.-P. Deng, and C. L. Henley, Phys. Rev. Lett. **63**, 310 (1989).

[16]K. J. Strandburg, L.-H. Tang, and M. V. Jarić, Phys. Rev. Lett. **63**, 314 (1989).

[17]J. E. S. Socolar, T. C. Lubensky, and P. J. Steinhardt, Phys. Rev. B **34**, 3345 (1986); J. E. S. Socolar, *ibid.* **39**, 10 519 (1989).

[18]P. Bak, Rep. Prog. Phys. **45**, 587 (1982).

[19]S. Aubry, J. Phys. (Paris) **44**, 147 (1983); in *Structure et Insta-*

bilité, edited by C. Godréche (Editions de Physique, Les-Ulis, 1986); p. 73; S. Aubry and P. Quemerais, in *Low Dimensional Electronic Properties of Molybdenium Bronzes and Oxides,* edited by C. Schlenker (Kluwer, Dordrecht, 1989), p. 295.

[20]J. Villain and M. Gordon, J. Phys. C **13**, 3117 (1980); F. Axel and S. Aubry, *ibid.* **14**, 5433 (1981).

[21]W. Selke and P. M. Duxbury, Z. Phys. B **57**, 49 (1984).

[22]C. S. O. Yokoi, L.-H. Tang, and W. Chou, Phys Rev. B **37**, 2173 (1988).

[23]A. M. Szpilka and M. E. Fisher, Phys. Rev. Lett. **57**, 1044 (1986); M. E. Fisher and A. M. Szpilka, Phys. Rev. B **36**, 644 (1987); **36**, 5343 (1987); A. M. Szpilka and M. E. Fisher, *ibid.* **36**, 5363 (1987).

[24]N. G. deBruijn, Proc. Konig. Ned. Akad. Weten. **A84**, 39 (1981).

[25]S. Ostlund and D. C. Wright, Phys. Rev. Lett. **56**, 2068 (1986).

[26]V. Elser, Phys. Rev. B **32**, 4892 (1985).

[27]M. V. Jarić, Phys. Rev. B **34**, 4685 (1986).

[28]P. Bak, Phys. Rev. Lett. **54**, 1517 (1985); Scr. Metall. **20**, 1199 (1986).

[29]J. D. Weeks and G. H. Gilmer, in *Advanced Chemistry and Physics,* edited by I. Prigogine and S. A. Rice (Wiley, New York, 1979), Vol. 40, p. 157.

[30]C. Rottman and M. Wortis, Phys. Rep. **103**, 59 (1984).

[31]H. van Beijeren and I. Nolden, in *Structures and Dynamics of Surfaces II,* edited by W. Schommers and P. von Blanckenhagen (Springer, Heidelberg, 1987).

[32]D. B. Abraham, in *Phase Transitions and Critical Phenomena,* edited by C. Domb and J. L. Lebowitz (Academic, London, 1986), Vol. 10, p. 1.

[33]D. Levine, T. C. Lubensky, S. Ostlund, S. Ramaswamy, and P. J. Steinhardt, Phys. Rev. Lett. **54**, 1520 (1985).

[34]M. V. Jarić and L.-H. Tang (unpublished).

[35]M. V. Jarić and U. Mohanty, Phys. Rev. B **38**, 9434 (1988).

[36]P. Bak, Phys. Rev. B **32**, 465 (1985).

[37]See, for example, L. W. Swanson, *Linear Programming: Basic Theory and Applications* (McGraw-Hill, New York, 1980).

[38]N. G. deBruijn, J. Phys. (Paris) Colloq. **C3**, 9 (1986).

[39]H. W. J. Blöte and H. J. Hilhorst, J. Phys. A **15**, L631 (1982).

[40]J. Villain and P. Bak, J. Phys. (Paris) **42**, 657 (1981); F. D. M. Haldane and J. Villain, *ibid.* **42**, 1673 (1981).

[41]K. J. Strandburg and P. R. Dressel (unpublished).

[42]F. Vallet, R. Schilling, and S. Aubry, Europhys. Lett. **2**, 815 (1986).

[43]R. Lipowsky and C. L. Henley, Phys. Rev. Lett. **60**, 2394 (1988).

[44]P. A. Kalugin, Pis'ma Zh. Eksp. Teor. Fiz. **49**, 406 (1989) [JETP Lett. **49**, 467 (1989)].

[45]J. É. S. Socolar, Commun. Math. Phys. (to be published).

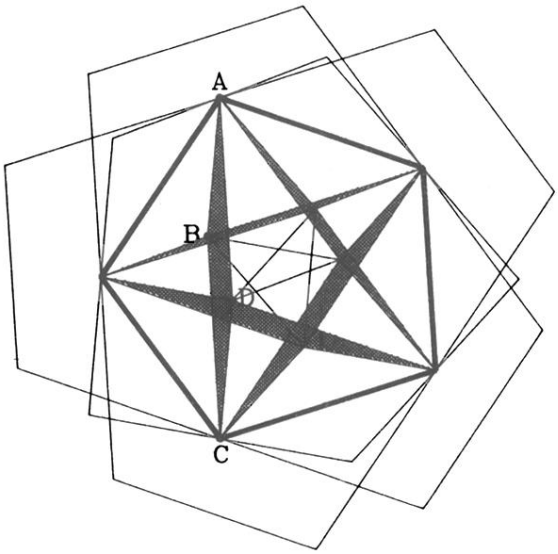

FIG. 25. Overlapping pattern of D_2 (region enclosed by the heavy lines) with other window domains for a strained tiling. The shaded area does not correspond to any of the subdomains on Fig. 24(b), thus representing vertices where the neighboring bond configuration is not found in a Penrose tiling.

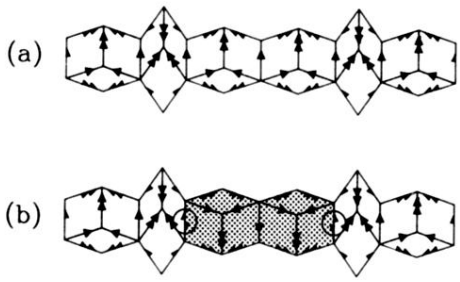

FIG. 5. (a) A worm formed by six hexagons. Edges on the two sides of the worm are decorated symmetrically. (b) The same worm with two hexagons (shaded) flipped. As a result, two $(SS)^{-}$ bonds, indicated by circles, are created.

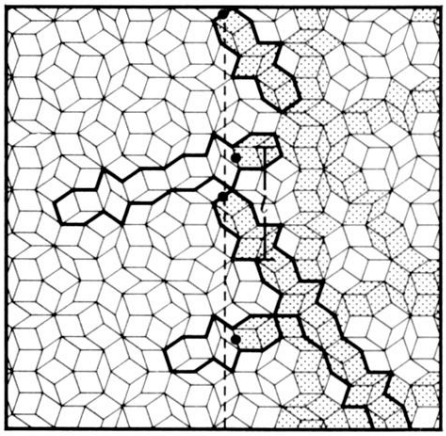

FIG. 6. Two Penrose tilings joined along the dashed line. The shaded tiles on the right-hand side must be rearranged if we are to continue the left Penrose tiling across the dashed line. Solid circles indicate $(SS)^{-}$ bonds. Worms running across the dashed line are indicated by the heavy lines. The typical interspacing of the network of flipped worms is l.

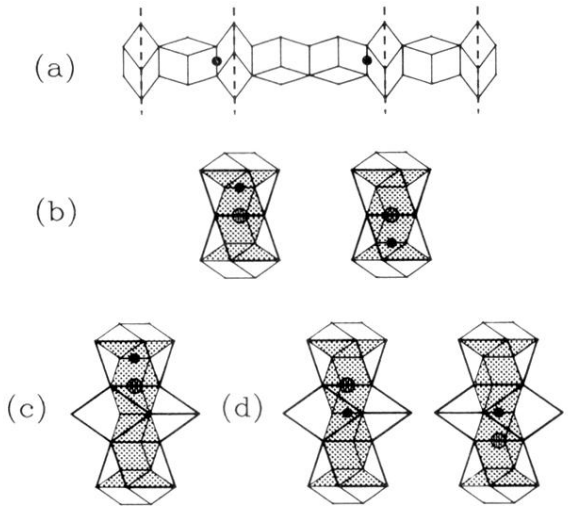

FIG. 9. (a) Dividing a worm into sections according to the arrangement of short hexagons. (b) Two possible configurations for sections containing one long hexagon and an $(SS)^{-}$ bond, along with bonds of the inflated pattern, as shown by the heavy lines. (c) A two-long-hexagon pattern containing an $(SS)^{-}$ bond which gives a unique inflated pattern. (d) Another two-long-hexagon pattern containing an $(SS)^{-}$ bond which gives two different inflated patterns, each assigned a probability $\frac{1}{2}$.